

POLITECNICO DI TORINO

Master Degree in Aerospace Engineering

Master Degree Thesis

**Experimental Investigation of Stator
Blade Vibration Due to Air Impingement
in a Axial/Centrifugal Compressor**



Supervisor

Prof. D. G. Pastrone

Candidate

Simona Rocchi

July 2020

*Ai miei genitori,
per aver fatto della mia felicità
il loro obiettivo*

Abstract

The purpose which has guided the integration and the development of the quick-start system is the increase of safety during intended single-engine operation for rotorcraft application, leading to an effective reduction of the start-up time of the inactive turboshaft engine. The acceleration torque provided by the system is obtained through a pressurized air injection at the compressor section using an impingement system made up by three de Laval nozzles, integrated into the impeller casing. During maintenance operations on the modified engine at the TUM laboratory, one blade of the last stator stage in the axial compressor has found damaged and the investigation of the possible causes related to this failure was the aim of this work of thesis. The attention has been focused on the vibration field originated by the quick-start system, which represents a very intense and exciting phenomenon for the whole compressor. In particular, during the working time of the quick-start system a reverse flow has sourced from the impeller section, leading to the excitation of the compressor blades. To analyze the effects of this excitement, a deep investigation has carried out, involving an initial numerical analysis, followed by several experimental tests. The first part of the analysis has involved the creation of a finite-element model of the blade, to find out its natural frequencies and obtain a visual investigation of the vibration modes. To proceed with the experimental investigation, two blades have been instrumented with the strain gauges connected in a half-bridge configuration. Besides, two vibration sensors have been placed on the compressor casing and two on the rear bearing. Since the amount of the originated backflow is strongly affected by the pressure reached in the impeller section, some pressure sensors have been installed at different points of the compressor section. The interpretation of the gained results has shown the strong influence of the quick-start system into the vibration field arose on both blades and compressor casing, and the frequency values associated with these phenomena. Although the integration of the quick-start system leads to an effective reduction in the starting time, the results have shown that its impulsive action impacts the life of the entire compressor. Additional workload involves the structure of blades, the compressor casing, and the bearing, mostly related to the appearance of fatigue phenomena, whose persistence over time strongly compromise the safety operations of the compressor.

Contents

1	Introduction	1
1.1	Motivation	2
1.2	Thesis Objective	4
2	State of The Art	5
2.1	Overall Performance of The Allison 250-C20B Turboshaft Engine	5
2.2	Quick-Start System	7
2.2.1	Design and Integration of the Air Impingement System	7
2.2.2	Air Supply System	9
2.2.3	Performance of the Quick-Start System	10
3	Analysis and Simulation of Blade Vibration	12
3.1	Overview of Different Vibration Types	13
3.1.1	Sinusoidal Signal	15
3.1.2	Quasi-Sinusoidal Stationary Signal	16
3.2	Concept of DOF	17
3.3	Simple Mass-Spring-Damper Vibration Model	18
3.3.1	Free Damped Vibration	19
3.3.2	Forced Vibration	21
3.3.2.1	Steady-State Harmonic Response	21
3.3.2.2	Impulse Response	24
3.3.3	Multiple Degree of Freedom System	25
3.3.4	Normal Modes Analysis	26
3.4	Numerical Analysis of the Stator Blade	27
3.4.1	Overview of Finite Element Process	27
3.4.2	Finite Element Model of the Stator Blade	29
3.4.3	Lanczos Eigensolver Method for the Eigenvalue Extraction	31
3.4.4	Mesh Refinement	31

3.4.5	Visualization of the Results	32
3.5	Selection of the Strain Gauge Placement	35
3.5.1	AutoMAC Criterion	35
4	Methods for Vibration Measurement	38
4.1	Blade Vibration Measurements	38
4.1.1	Overview of Linear Elasticity	39
4.1.2	Strain Gauge: Features, Measuring Circuit and Applications	41
4.1.2.1	Strain Gauge Measurement: Wheatstone Bridge	43
4.1.2.2	Bridge Configuration on the Blade	46
5	Configuration of the Test Rig and Procedure	48
5.1	Mechanical Integration of the Compressor Section	48
5.2	Measurement Devices	51
5.2.1	Vibration sensors	51
5.2.2	Pressure Sensors	55
5.2.3	Thermocouple for Temperature Measurement	55
5.2.4	Measurement of Rotational Speed	56
5.3	Data Acquisition System	57
5.4	Experimental Procedure	58
6	Investigation of the Results	60
6.1	Stator Blade Experiments	60
6.1.1	Results from Static Tests	62
6.1.2	Results from Dynamic Tests	65
6.1.3	Evaluation of the Results	67
6.2	Compressor Section Experiments	69
6.2.1	Results Reporting	70
6.2.2	Evaluation of the Results	76
7	Summary and Outlook	78

List of Figures

1.1	Fuel saving potential due to use of ISEO at appropriate flight operation . . .	1
1.2	Bottom part of the stator casing where the broken of the blade has occurred	3
2.1	Section view of the Allison 250-C20B Turboshaft Engine [14]	5
2.2	Schematic diagram of the Allison 250-C20B Engine [7]	6
2.3	Model of the impeller casing integrated with AIS components [7]	8
2.4	Impeller casing with the integrated five air supply pipes and its inclusion into the compressor section [11]	8
2.5	Scheme of the Quick-Start System which shows the components of both Air Supply System and Air Impingement System	10
2.6	Comparison of the GG spool speed reached into the engine with an electric starter and with the addition of the QSS [7]	11
3.1	Representation of the Sine function for different phase angle values	15
3.2	Representation of a quasi-sinusoidal stationary signal	16
3.3	Examples of simple systems with a single degree of freedom	17
3.4	Examples of simple systems with two degrees of freedom	18
3.5	System characterized by one degree of freedom which is the output displacement $y(t)$	18
3.6	Investigation of the over-damped $\zeta > 1$, critically-damped $\zeta = 1$ and under-damped $\zeta < 1$ vibration [17]	20
3.7	Magnitude of the frequency response function for the displacement	23
3.8	Angle of phase lag of the displacement response	23
3.9	Scheme of the analysis process computed in Abaqus	28
3.10	Preprocessing of the Blade Finite Model	29
3.11	Geometry of the stator blade created with CATIA	30
3.12	Mesh adopted for the discretization of the stator blade	32
3.13	First vibration mode obtained from the FE-analysis which displays the bending deformation of the blade	33

3.14	Second vibration mode obtained from the FE-analysis which displays the torsional deformation of the blade	34
3.15	Third vibration mode which displays the coupling between the bending and torsion deformation of the blade	34
3.16	Fourth vibration mode obtained from the FE-analysis	34
3.17	Fifth vibration mode obtained from the FE-analysis	34
3.18	AutoMAC Matrix which displays the degree of correlation existing between the first ten natural modes	36
4.1	Effect of a tensile force applied in both sides of the body	40
4.2	Structure and components of the metal foil strain gauge [6]	42
4.3	Effect of tensile/compressive load on the cross section	42
4.4	Temperature effect on the gauge factor [6]	43
4.5	Electrical Scheme of a full Wheatstone bridge	44
4.6	Quarter Bridge with the resistance R1 affected by tension load, leading to $\epsilon_1 < 0$	45
4.7	Quarter Bridge with the resistance R2 affected by compression load, leading to $\epsilon_2 > 0$	45
4.8	Electrical scheme of the half bridge configuration	46
4.9	Configuration of the strain gauges for a bending beam	46
4.10	Electrical scheme of the bridge installed on the blades for the vibration measurements	47
5.1	Lateral view of the integrated compressor section	49
5.2	Rear view of the integrated compressor section	49
5.3	Final setup of the compressor section with all the parts and sensors integrated	50
5.4	Final configuration of the test rig, showing both the compressor section and the QSS	51
5.5	Vibration Transducer type 4–123 [5]	52
5.6	Industrial Accelerometer IEPE iCS80 [9]	53
5.7	Relative orientation of the sensors placed on the rear bearing and on the compressor casing	54
5.8	Final integration of the test rig with the installed sensors on the bearing and the compressor casing	54
5.9	Circuit for temperature measurement with type K-thermocouple	56
5.10	PICOTURN-BM V6 controller [1]	57

6.1	Comparison of the impeller relative static pressure reached during the static tests S1, S2 and S3	62
6.2	RMS comparison for the static tests S1,S3 and S4	63
6.3	Result of the Fast Fourier Transform computed for test S1	64
6.4	Result of the Fast Fourier Transform computed for test S3	64
6.5	Result of the Fast Fourier Transform computed for test S4	64
6.6	Amplitude comparison between the vibration acquired by the longitudinally and the transversely placed strain gauges	65
6.7	Trend of the speed curve and vibration amplitude for the dynamic test D1	65
6.8	Result of the Fast Fourier Transform evaluated for the test D1	66
6.9	Vibration amplitude regarding dynamic text D2	66
6.10	Fast Fourier Transform computed for the dynamic test D2	67
6.11	Compressor casing vibration acquired by the horizontal and the vertical sensors during the dynamic test D001	71
6.12	Rear bearing vibration acquired by the horizontal and the vertical sensors during the dynamic test D001	71
6.13	Fast Fourier Transform computed for the vibration acquired by the horizontal sensor placed on the compressor casing	72
6.14	Fast Fourier Transform computed for the vibration acquired by the vertical sensor placed on the compressor casing	72
6.15	Fast Fourier Transform computed for the vibration acquired by the horizontal sensor placed on the rear bearing	72
6.16	Fast Fourier Transform computed for the vibration acquired by the vertical sensor placed on the rear bearing	72
6.17	Relative static pressure reached in the impeller outlet section during the static test S001 and the dynamic test D001	73
6.18	Vibration amplitude comparison between the static test S001 and the dynamic test D001	73
6.19	Fast Fourier Transform computed for the static test S001	74
6.20	Fast Fourier Transform computed for the dynamic test D001	74
6.21	Comparison of the reached impeller static pressure during the static tests S001, S002 and S003	74
6.22	Comparison of the vibration amplitude affected the compressor casing during the static tests S001, S002 and S003	74
6.23	Fast Fourier Transform computed for the static test S001	75
6.24	Fast Fourier Transform computed for the static test S002	75
6.25	Fast Fourier Transform computed for the static test S003	75

6.26 Comparison between the vibration amplitude of the casing for the dynamic tests D002 and D003	75
6.27 Fast Fourier Transform computed for the dynamic test D002	76
6.28 Fast Fourier Transform computed for the dynamic test D003	76

List of Tables

2.1	Specifications of the Engine Allison 250-C20B [24]	7
2.2	Number of blades and vanes in the compressor section [10]	7
2.3	List of the AIS components integrated into the impeller section	8
2.4	Main parameters of the QSS [11]	9
3.1	Resulting natural frequencies of the blade FE model	33
5.1	List of the new integrated parts into the compressor section	49
5.2	List of the parts integrated into the compressor section	50
5.3	List of the ASS parts integrated in the final test rig configuration	51
5.4	List of the vibration sensors mounted on the bearing and on the compressor casing	53
6.1	List of the conducted static tests and their characteristic parameters	61
6.2	List of the conducted dynamic tests and their characteristic parameters	61
6.3	List of the static tests conducted for the evaluation of the vibration on the compressor casing and rear bearing	69
6.4	List of the dynamic tests conducted for the evaluation of the vibration on the compressor casing and rear bearing	70

Nomenclature

Latin Symbols

A	$[m^2]$	Area
c	$[\frac{Ns}{m}]$	Damping
C	$[m]$	Arbitrary constant
E	$[Pa]$	Young's modulus
f	$[Hz]$	Frequency
F	$[N]$	Force
G	$[\frac{m}{N}]$	Transfer function
k	$[\frac{N}{m}]$	Stiffness
l	$[m]$	Displacement movement
L	$[m]$	Length
m	$[kg]$	Mass
\dot{m}	$[\frac{kg}{s}]$	Mass flow rate
$N1$	$[RPM]$	Gas generator spool speed
$N2$	$[RPM]$	Power output shaft speed
P	$[W]$	Power
R	$[\Omega]$	Resistance
S	$[m]$	Mode shapes
t	$[s]$	Time
T	$[s]$	Time period
V	$[V]$	Voltage
y	$[m]$	Displacement

Greek Symbols

α	$\left[\frac{V}{K}\right]$	Seebeck's coefficient
γ	$[-]$	Shear strain
δ	$[N]$	Dirac function
ϵ	$[-]$	Strain
ζ	$[-]$	Damping ratio
Θ	$[K]$	Temperature
κ	$[-]$	Gauge factor
λ	$\left[\frac{1}{s}\right]$	Eigenvalue
μ	$[Pa]$	Shear modulus of elasticity
ν	$[-]$	Poisson's coefficient
ρ	$[\Omega * m]$	Resistivity
σ	$[Pa]$	Stress
τ	$[Pa]$	Shear stress
φ	$[rad]$	Phase angle
ϕ	$[m]$	Eigenvector
Φ	$\left[\frac{m}{s}\right]$	Indefinite integral
ω	$\left[\frac{rad}{s}\right]$	Pulse

Abbreviations

AEO	All Engines Operation
AIS	Air Impingement System
ASS	Air Supply System
ESPSS	European Space Propulsion System Simulation
FADEC	Full Authority Digital Engine Control
FEA	Finite Element Analysis
FF	Fuel Consumption
FFT	Fast Fourier Transform
GG	Gas Generator
GI	Ground Idle
HPC	High Pressure Compressor
HPT	High Pressure Turbine
ISEO	Intended Single Engine Operation
LPT	Low Pressure Turbine
LTF	Lehrstuhl für Turbomaschinen und Flugantriebe
MDOF	Multiple Degree Of Freedom
QSS	Quick-Start System
SFC	Specific Fuel Consumption
SDOF	Single Degree Of Freedom
TUM	Technical University of Munich

Chapter 1

Introduction

For safety reasons, most helicopters are equipped with two or more turboshaft engines mainly operating in part-load conditions. This results in high specific fuel consumption (SFC), which could be reduced by increasing engine load: shut-off of one engine in suitable flight envelope areas could lead to a significant reduction in the overall consumption of up to 30%, compared to conventional operation [4]. This can be seen in Fig 1.1, that shows the differences between intended single-engine operation (ISEO) and all engines operation (AEO) for the Bluecopter Demonstrator of Airbus Helicopters. The maximum output power of the used engine is 500 kW, which represents the ISEO limit. The red curves display the trend of the specific fuel consumption (SFC) and the fuel consumption (FF) in the function of delivered power for ISEO mode, denoting an effective reduction of fuel consumption, compared to the blue ones, related to the twin-engine helicopter.

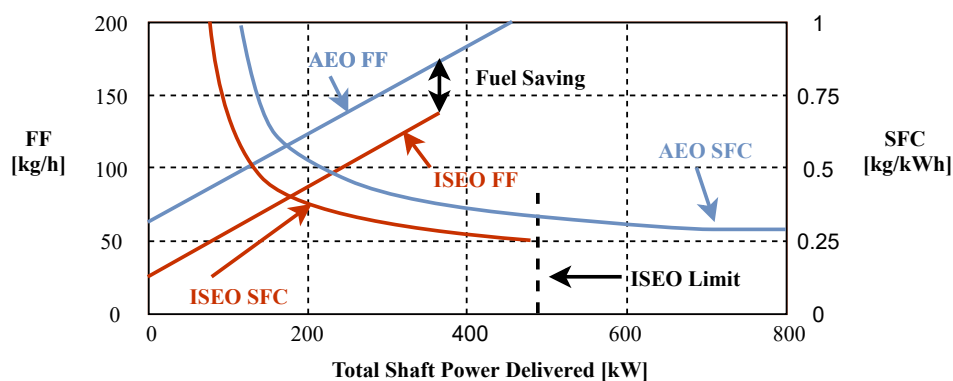


Figure 1.1: Fuel saving potential due to use of ISEO at appropriate flight operation [13]

In case of failure of the engine during intended single-engine operation, the inactive engine requires from 25 s to 28 s to reach ground idle speed and during this interval, the helicopter loses an overall height of 400 m-550 m [23]. An approach to minimize the height loss is

reducing the start time of the inactive turboshaft engine. Rapid starting, to improve the emergency condition for ISEO, can be accomplished by applying an additional acceleration torque for the gas generator (GG) provided by a technical device. The investigation of various methods of applying high cranking energy has involved several years of research. Hull and Santo in the remote 1967 have investigated the following possible energy sources [8]: electric motor, pneumatic motor, hydraulic motor, inertia system, hydrazine impingement and cartridge impingement. Although the possibility of achieving a huge reduction in the start-up time was proved, all these solutions have revealed many drawbacks like costs, complexity, excessive additional weight, and much installation space. Some years later the idea of a pneumatical system was introduced, based on high-pressure air or hot-gas impingement from supplementary nozzles [22]. At the beginning the gas impingement was in the turbine section, leading to an overall low acceleration of the GG, due to turbine design and its operational principle. A gas impingement at the compressor section was also investigated and after several tests conducted with compressed nitrogen, this was the proper solution, with the lowest reasonable cost and feasibility [22].

Based on these previous investigations, to ensure full power delivering in the shortest time, the Chair of Turbomachinery and Flight Propulsion (LTF) at the Technical University of Munich (TUM) has developed a quick start system (QSS) with air injection instead of nitrogen. For QSS proof of concept tests, a turboshaft engine was chosen, therefore, the instrumented and fully functional Allison 250-C20B turboshaft engine of the Institute was a reasonable choice. Thus, the system was designed and experimentally investigated for this family of turboshaft engine, made up of an axial compressor with six stages combined with a single-stage radial compressor, available at the TUM testbed. The QSS accelerates the compressor engine through an air impingement system, which includes three De Laval Nozzles, asymmetrically distributed around the impeller circumference, and a pressurized air bottle.

1.1 Motivation

The purpose which has guided the integration and the development of the QSS is the increasing of safety during ISEO, for this reason, several experimental tests were conducted at the TUM testbed, getting an effective reduction of the start-up time. Introducing this system, without a complete deterioration of the performance and with a slight modification of the impeller casing, the start-up time was reduced of approximately 90% [7].

During maintenance operations on the modified engine, one blade of the last stator stage in the axial compressor was found damaged. As shown in Fig 1.2, representing the bottom

half of the compressor casing, the damage occurred in the stator has led to the loss of the blade. This breakup has compromised the further use of the blade since it cannot perform its intended function safely, leading, in addition to a deterioration of the engine performances.

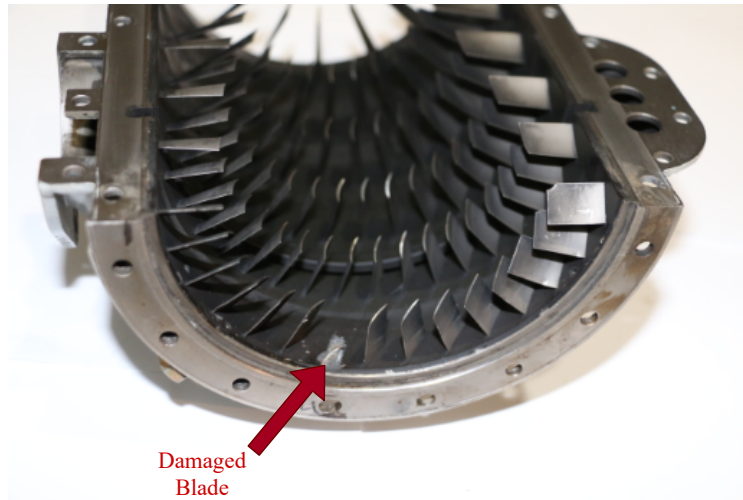


Figure 1.2: Bottom part of the stator casing where the broken of the blade has occurred

More generally, both rotor and stator blades of compressor experience severe aerodynamic, mechanical, and thermal loads in service, interacting directly with the fluid to promote energy transfer. The loads that mostly act on a turbomachine blade are the following: direct and indirect fluid loads, centrifugal force due to shaft rotation, and cyclic loads caused by machine vibration [2]. In addition to these, the blades are exposed to other possibilities of damage like erosion or abrasion, cavitation, corrosion due to the fluid or contaminants and high temperature creep. Despite all these factors affect and limit the blade performance, the broken fracture is seldom related to the energy transfer loads, since it is mostly connected with blade resonance phenomena. For the engine under analysis, equipped with the QSS, one of the forces responsible for the vibration field is correlated with the backflow that arose from the impinged amount of air. Due to this, the compressor is submitted to further stress, acting as an impulse force on the vane's surface.

The goal set in this work of thesis is the deep investigation of the vibration field caused by this impingement force, as the possible main cause of the fail. To this aim the analysis was conducted involving a numerically investigation of the blade behaviour followed by experimental tests.

1.2 Thesis Objective

As it stands from the title, this work intends an experimental investigation of the vibrations, to analyze and thus prevent the causes that have lead to the damage of the blade. In particular, the attention is focused on the effects originated due to the integration of the QSS into the engine, in order to find out the possible correlation between the failure and the impingement system.

At the beginning it was deemed of primary importance, an analytical and numerical analysis of the problem, to set the requirements for the experimental investigations. For this reason, the work begins with an analytical investigation of the force originated from the backflow and acting on the blade. Its computation provides information on the intensity of the impingement force and its main determinants. To gain a preliminary understanding of the blade vibration modes and their natural frequencies, a numerical analysis was conducted. For this purpose, a Finite Element Model of the blade was realized and investigating the results acquired from the simulation, a visual examination of the nodal displacement and the strain was also carried out. The experimental part has been preceded by a preparation phase, concerning the setup of all the components employed during the experiments. First of all, the integration of the compressor section. To narrow the investigation field to the effect of the quick start system only, the tests are restricted on the axial compressor section, including the axial and centrifugal compressor, neglecting the combustion chamber and the turbine section. An existing test rig of the compressor was used, to which new design parts have been added. For the acquisition of the measurements, a set of sensors was installed: to this aim, the stator blade was instrumented with the strain gauges; several pressure sensors were placed on the compressor section and vibration sensors were installed on the compressor casing and the rear bearing. Besides a speed sensor was set to detect the rotational speed. All the connections between these local detection devices and the data acquisition systems were realized through a system of cables with which the signal is conveyed. Once the experimental tests were completed, the results were shown through a display system and after numerically evaluated.

Chapter 2

State of The Art

In this chapter, relevant details and specifications concerning the Allison 250-C20B engine and the QSS design are provided. Mainly, the attention is focused on the compressor section, highlighting the modifications included due to the integration of the impingement system into the impeller casing.

2.1 Overall Performance of The Allison 250-C20B Turboshaft Engine

The Allison 250-C20B is a family of turboshaft engine, developed by The Allison Engine Company in the early 1960s and produced later by Rolls Royce. The wide family product is used for turboprop, turboshaft, and marine starter application. The turboshaft applications include the Bell 206B/TH-67, MDH MD500/520N, and Eurocopter AS.355/BO 105 [14]. In Fig 2.1 is displayed a section view of the engine with its main components, below described more in detail.

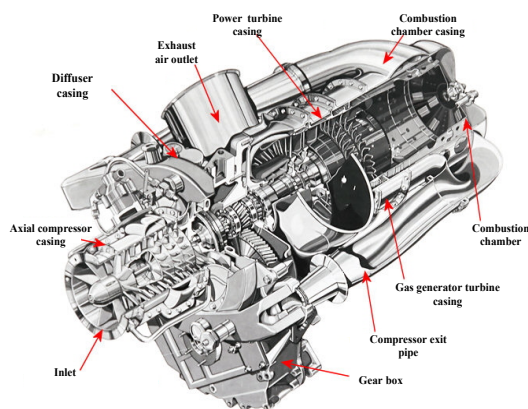


Figure 2.1: Section view of the Allison 250-C20B Turboshaft Engine [14]

In order to understand the components of the engine and the airflow through it, the following description is provided. As shown from the schematic representation in Fig 2.2, an airflow rate of $1.56 \frac{kg}{s}$, depicted with the blue color, is channeled into the engine, through a frontal inlet, facing with the first stage of the high-pressure compressor (HPC): it has an axial-radial design and consists of a six-stage axial compressor and a final radial compressor stage. At the tip of the fifth rotor stage, there is a bleed valve for the air extraction to prevent the engine from surge at low rotational speeds.

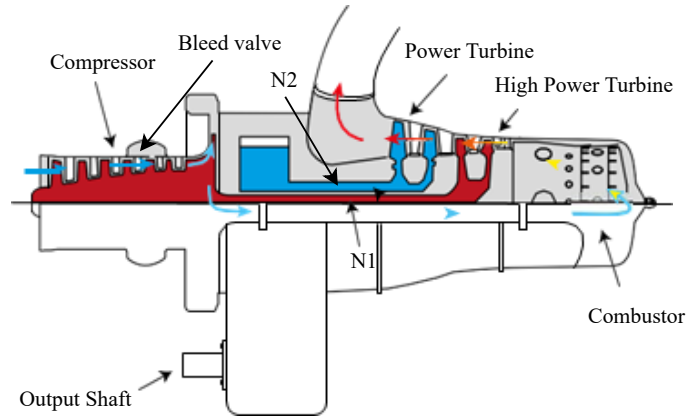


Figure 2.2: Schematic diagram of the Allison 250-C20B Engine [7]

The compressed air is guided by two pressure lines into the combustion chamber, where the fuel is injected into the flow and the mixture is burned. The engine has two spools and its modular design enables an easy exchange of engine parts. The central mounting part of the engine is the gearbox and all turbine shafts are stored in it. The turbine consists of a two-stage axial low-pressure turbine (LPT) and a two-stage axial high-pressure turbine (HPT). The HPT is mounted on the GG shaft and drives the HPC. Via the gearbox, it drives the auxiliaries such as oil pump, fuel pump, or starter generator. It is followed by the LPT, or Power Turbine mounted on the power consumer output shaft (e.g. the helicopter rotor). This free turbine is connected to the accessory gearbox, which gears down its speed (N2) to a more manageable level. Via these low-pressure stages, the fluid is further expanded and leaves the engine through piping in the radial direction to the shafts [14].

The most relevant parameters of the engine at standard sea level conditions are listed in the following Tab 2.1:

Table 2.1: Specifications of the Engine Allison 250-C20B [24]

Maximum Continuous Power	P_{max}	298 kW
Take-off Power	P_{TO}	313 kW
Maximum Speed GG Shaft	$N1_{max}$	53000 $\frac{1}{min}$
Maximum Speed Geared Output Shaft	N_{out}	6016 $\frac{1}{min}$
Maximum Speed Power Output Shaft	$N2_{max}$	33290 $\frac{1}{min}$
Specific Fuel Consumption	SFC	396 $\frac{g}{kWh}$
Airflow Rate	\dot{m}_{air}	1.56 $\frac{kg}{s}$

The compressor is located in a split stainless steel housing with an overall length of 22 cm and the number of blades characterizing the stator and rotor of each row is listed in the following Tab 2.2:

Table 2.2: Number of blades and vanes in the compressor section [10]

Rotor Row	R1	R2	R3	R4	R5	R6	R7 (Impeller)
Number of Blades	16	16	20	25	28	25	28
Stator Row	S1	S2	S3	S4	S5	S6	S7 (Diffuser)
Number of Vanes	14	26	28	32	36	30	16

2.2 Quick-Start System

As previously proposed, an approach to minimize the loss of height, to increase the safety of ISEO, is reducing the start time of the turboshaft engines, through the integration of the QSS. The following treatment intends to provide more details regarding this integration into the compressor impeller and also the specifications of its subsystems: the air impingement system (AIS) and the air supply system (ASS).

2.2.1 Design and Integration of the Air Impingement System

The AIS involves the modified impeller casing, where the impingement nozzles and the relative supply pipes have been integrated. The integration of the QSS entails only the radial compressor unit, as shown from Fig 2.3, which displays the new designed aluminum

casing C1, including the elliptic hole of the nozzle C2, and the de Laval nozzle C3, listed in Tab 2.3. The circular cross-section of the nozzles, installed at an angle of 25° leads to elliptic holes in the inner surface of the casing, as depicted in Fig 2.3.

Table 2.3: List of the AIS components integrated into the impeller section

Nr	Component
C1	Modified impeller casing
C2	Elliptic hole of the nozzle
C3	De Laval Nozzle

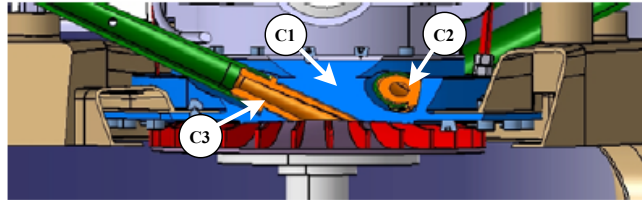


Figure 2.3: Model of the impeller casing integrated with AIS components [7]

The casing of the radial compressor has been equipped with five impingement de Laval nozzles asymmetrically positioned at a radius and an angle able to provide the highest effect on the acceleration of the impeller and thus of the complete GG. The optimum count of five nozzles was defined considering the restriction due to space and the start performance calculations. Also, this distribution avoids both, collision with accessories and harmonic excitation of the blades [7]. In this initial configuration, the shop air for nozzle supply has a static pressure of 13 bar. The following Fig 2.4 shows in the left side, the main components of the AIS integrated in the modified impeller casing and in the right side the inclusion of this system into the engine.

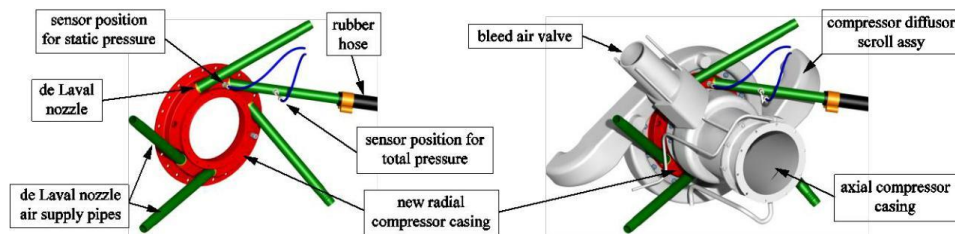


Figure 2.4: Impeller casing with the integrated five air supply pipes and its inclusion into the compressor section [11]

Since weight saving is an important factor, a new configuration of the system with only three active nozzles was developed, although this new configuration leads to a slight in-

crease in the consumption during the operating time, due to its lower efficiency.

To obtain the same improvement concerning the start-up time, the nozzle entry total pressure has to be increased. To this aim, the conducted simulations have revealed that a nozzle entry total pressure of about 18 bar needs to be used in the three nozzles configuration [12]. For what concerns the geometrical features of the nozzle, the nozzle throat diameter is 6.6 mm which means an air mass flow of 0.15-0.17 kg/s, resulting in 0.5 kg/s overall air mass flow. Other relevant parameters regarding the period of operation of the QSS are provided by the following Tab 2.4:

Table 2.4: Main parameters of the QSS [11]

Air velocity at nozzle exit	Mach 2.3
Nozzle entry total pressure	18 bar
System deactivation limit	57% GG spool speed
System active time	2.2 s

2.2.2 Air Supply System

The configuration of the system made up of three active nozzles, has led to a reduction of the weight and an increase of the nozzle entry pressure, keeping in this way the same acceleration times. This affects the nozzle thrust, which is increased from 50 N to 83.5 N [12]. The simulations, performed with the ESPSS, have shown that this level of thrust is achievable with a nozzle entry pressure equals to 18.3 bar. Due to the measurement inaccuracies and assumptions, the ASS has to provide a nozzle entry total pressure level of 24-25 bar.

The design of the QSS employed for the experimental tests is shown in Fig 2.5, which depicts the air supply system, the air impingement system, and their connections. Referring to this figure, the main components and their function are described.

A three-way (1/3) air distribution manifold block is required to feed each nozzle of the AIS from one supply line. The manifold block is directly connected upstream to a coaxial valve, which releases the pressurized air into the nozzles. This valve is equipped with a piston, moved through electromagnetic forces, and in a very short opening time, below 100 ms, the maximum flow rate through the valve is obtained. Thus, this kind of valve represents a suitable solution in terms of weight and safety [12].

The pressurized air is provided by a compressed air bottle, containing air at 300 bar and filled with a compressor before each experiment. An important component of the ASS

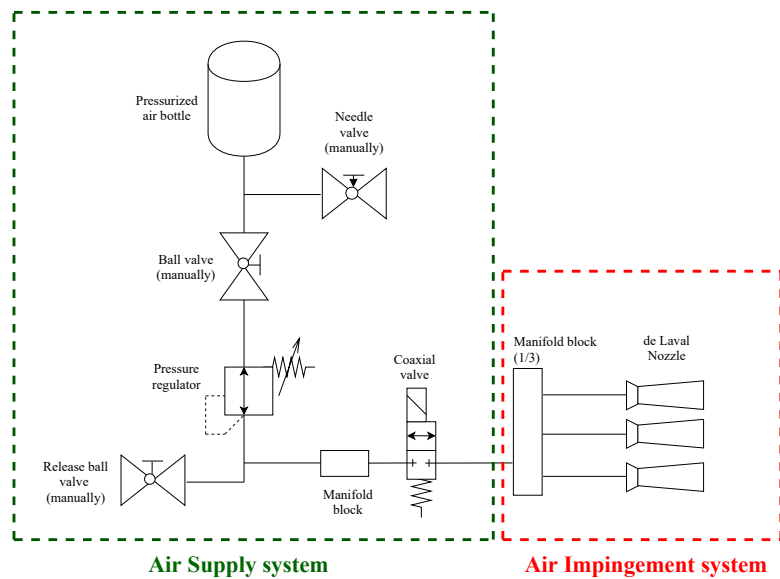


Figure 2.5: Scheme of the Quick-Start System which shows the components of both Air Supply System and Air Impingement System

is the pressure regulator, which can handle the high-pressure level of the pressurized air storage device and reduces it to the value required by the nozzles. The inlet pressure value into the pressure regulator is around 300 bar and the outlet pressure around 20-40 bar, higher than 18 bar, required by the nozzles, due to the further downstream total pressure losses [12]. The control of the QSS is integrated into the engine controller.

2.2.3 Performance of the Quick-Start System

The overall QSS operation time is approximately 2.2 s. The tests conducted on the engine integrated with the QSS show that the engine is ignited safely and accelerated to GI speed (60% of design GG speed) within 2.4 s instead of 26 s. This reduction in the start-up time is displayed in Fig 2.6, which shows two curves: the blue one, concerns the acceleration of the engine using only an electric starter and in this case, the GI speed is reached in 26 s. The green curve is related to the acceleration of the engine including both an electric starter and the nozzle system. After 2.42 seconds, the engine reaches the GI speed, leading a reduction of 90% in the start-up time. These results underline the high potential of the QSS, which allows a reduction of height loss from 400-500 m to 150-200 m [7].

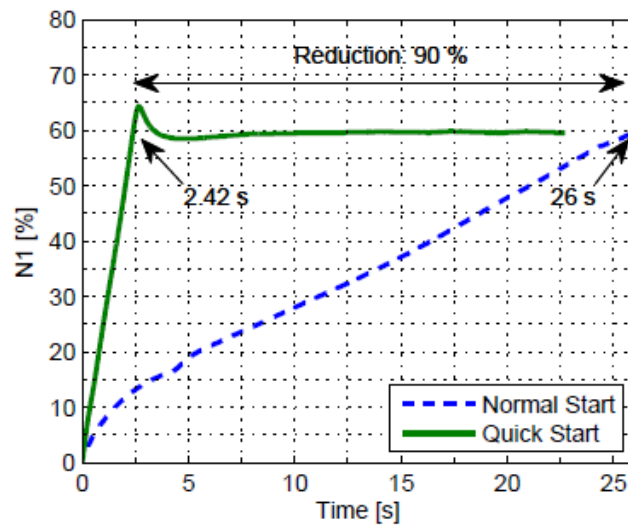


Figure 2.6: Comparison of the GG spool speed reached into the engine with an electric starter and with the addition of the QSS [7]

Chapter 3

Analysis and Simulation of Blade Vibration

Vibrations exist everywhere and impact the proper functioning of several elements: mechanical tools, engines or electric motors; electronic devices of different size and use; civil constructions like buildings and bridges and many others. Although sometimes their effects are positive, in most cases, the arising of vibration phenomena compromise the functionality. They can affect the normal behaviour, causing forced arrest and failures, in particular, unintended and durable vibrations may lead to catastrophic events, more serious in case of vibrations with high amplitude and compatible with resonance events.

In turbomachinery field, the analysis of blade vibration is an important task, in order to avoid the risk of blade failure due to the overcoming of fatigue limit. Both compressors and turbines typically consist of several stages of blades and vanes that are preliminarily designed for optimal aerodynamics performances. The blades in jet engines are subject to extreme loads, originated from the internal working fluid and also from further systems, many of which can cause vibrations that stress the components throughout all the operations.

Since it is turned out to be very important understanding both the cause of the vibrations and the response of the blades, this initial part of the work of thesis is focused on the analysis of the vibration field caused by the air impingement system, part of the QSS, as a possible cause of the failure of the stator blade. In addition, the investigation of the vibration modes of the blade and the search of its natural frequencies is essential for the following experimental tasks, to avoid useless tests.

To accomplish this aim, the analysis has started with an analytical approach based on numerical calculations of the impingement force, acting on the blade, and with a Finite Element simulation, to determine the shape modes of the blade and their related eigenfre-

quencies. Thus, the behaviour of the blade is analyzed in full extent using the commercially available finite element solver, Dassault Systemes Abaqus. One of the most dangerous occurrences, due to born of vibrations, is the appearing of resonance phenomena between the frequency of the exciting force and the natural frequencies of the blade. In order to investigate which are the most valuable parameters affecting the resonance, it is provided the analysis of the frequency response function, emphasizing its relevance inside the forced vibration field.

After acquiring the mode shapes, in the final part of this analytical phase, was used the autoMAC criterion to compare all the possible combinations between modes, highlighting their degree of correlation, to deal with possible overlapping during the setting of the measurement instruments.

3.1 Overview of Different Vibration Types

Vibration is an oscillatory and periodic motion which involves machines and structures and occurs around an equilibrium point [20]. Vibration can arise only applying a fluctuating force which may vary in magnitude and direction: this solicitation, able to cause vibration, is called exciting force or disturbing force. There are several types of vibration phenomena distinguishable due to the different nature of this force responsible for the vibratory motion. Among the variety of the phenomena the attention is more focused on the closest to this work, now briefly introduced:

- **Free Vibration:** They occur when a mechanical system is set in motion with an initial input and after allowed to vibrate freely [20]. It is performed under the action of forces inherent in the system itself without the intervention of fluctuating external forces of any kind. It will be shown later that the frequency of the free vibration typical of each system, called natural frequency, increases with the increasing of the spring stiffness and with the decreasing of the mass of the system.
- **Forced Vibration:** Differently from what just said, in this second case, the system is put in motion with a fluctuating force, that leads to an initial phase with irregular oscillations, thus called transient vibration. After the action of the viscous damping, only a steady-state vibration persists. The amplitude and frequency of the vibration depend on the applied force, in particular, the body is forced to vibrate at the same frequency of the excitation [20].

Next to these deterministic phenomena, it is also possible to face with random vibration: they can have varying waveform that not allow to predict the future behavior. Mostly,

all the vibrations of the real world belong to this class (e.g vibration from automobiles, aircraft).

The vibration phenomena have a periodic behavior, leading that the oscillations repeat themselves after a certain interval of time: this is called the period of the vibration, T [21]. Two other characterizing parameters are the frequency, f and pulse ω . Between them the following relations subsist:

$$\omega = 2\pi f = \frac{2\pi}{T} \quad \left[\frac{\text{rad}}{\text{s}} \right]$$

$$f = \frac{1}{T} = [\text{Hz}] = [\text{s}^{-1}]$$

Before to move on the investigation of vibration phenomena, it is appropriate to briefly examine the different types of signal existing in nature. The first possible classification is related to the way in which they affect structures and the type of damage connected with them. There are stationary vibration type phenomena, whose originated mechanical oscillation have a long time compared the exciting signal and shock type signals. In this second case the transient mechanical oscillation has a short period and they mostly cause aperiodic phenomena. Due to these differences they have a different impact on the behavior of the exciting element. The presence of stationary oscillations is responsible of mechanical fatigue stored and thus impact the operational modes over the lifespan. Shocks, for their intensity, lead in short time to a sudden damage.

In the subsequent analysis the attention is focused more on stationary phenomena, since it was assumed that the damage of the stator blade is more attributable to fatigue-related phenomena than to a sudden rupture.

Typical modelling of stationary phenomena is with a stationary-periodic sinusoidal signal, defined as a periodic movement whose main features are described below, in Fig 3.1. This is only an ideal model, which doesn't reflect the phenomena existing in nature. What happens in reality is more complicated, since, the mechanical vibrations, affecting the real components derive from an overlap of numerous signals, with different amplitudes and properties, resulting in the end in a more complicated displacement function with respect to time. Some examples of these real phenomena are: quasi-sinusoidal stationary signals, complex signals, random stationary/non-stationary signals and transitory signals.

3.1.1 Sinusoidal Signal

Among the periodic-stationary signals, the simplest one is the rectilinear sinusoidal movement, characterized by a sinusoidal elongation in function of time, $y(t)$, described through the following relation and displayed in Fig 3.1:

$$y(t) = y_{max} \sin(\omega t - \varphi) \quad (3.1)$$

Where:

y_{max} is the peak value or amplitude of the signal

ω is the pulse

φ is the phase angle at time $t = 0$: its positive/negative sign represents respectively an advance or a delay of the motion in time domain, as shown in Fig 3.1, which represents the sine function for three different values of phase angle.

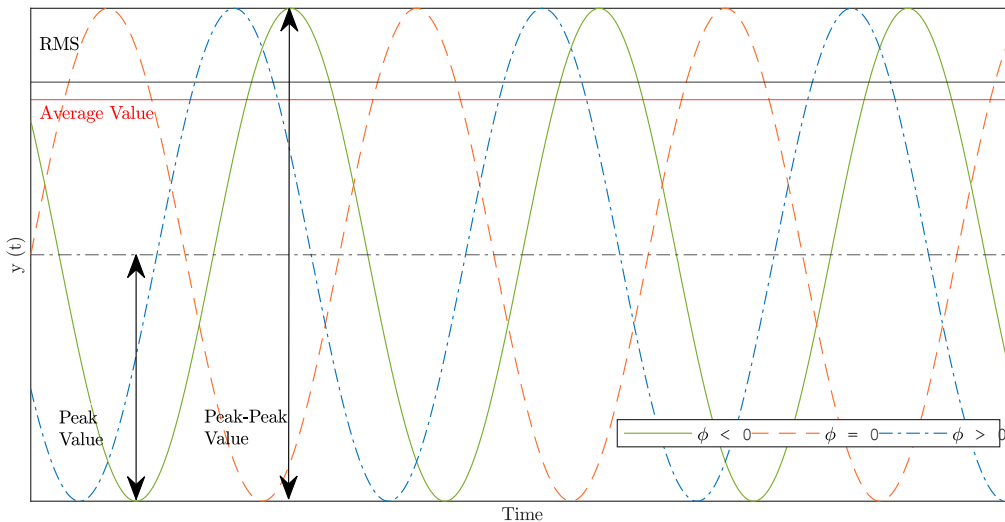


Figure 3.1: Representation of the Sine function for different phase angle values

Considering the relations between frequency, pulse and time above mentioned, the Eq 3.1 can be written as follow:

$$y(t) = y_{max} \sin(2\pi ft - \varphi) = y_{max} \sin\left(\frac{2\pi t}{T} - \varphi\right) \quad (3.2)$$

Several values are used to describe this basic signal, shown in Fig 3.1:

- Peak Value: it is defined as the maximum value from the point of balance [19]

- Peak to Peak Value: it characterizes the amplitude between positive and negative peak in a period, therefore defined as $2y_{max}$
- Average Value:

$$\overline{y(t)} = \frac{1}{T} \int_0^T y(t) dt$$

- True effective Value or Root Mean Square: this value is directly connected with the average power contained in the signal and for a continuous function it is defined as [19]:

$$y_{rms} = \sqrt{\frac{1}{T} \int_0^T y^2(t) dt}$$

In order to understand the meaning of this important value, it is possible to consider the analogy with electricity, where this is the value of a direct current that would dissipate the same power, in a passive resistive load, of the alternating signal $y(t)$ [19]. For the sinusoidal signal the following relation subsists between the amplitude and the root mean square value:

$$y_{rms} = \frac{y_{max}}{\sqrt{2}}$$

3.1.2 Quasi-Sinusoidal Stationary Signal

These kind of signals are very common in nature among the quasi-stationary phenomena and they are generally composed of a mixture of sinusoidal signals of constant amplitude, without harmonic relation among them. A representation of this type of signal is provided by the following Fig 3.2.

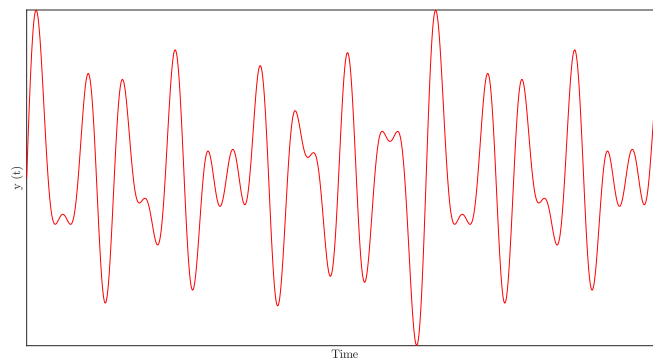


Figure 3.2: Representation of a quasi-sinusoidal stationary signal

The final resulting signal can be obtained by the addition or multiplication of several sinusoidal signals [19]. A generic analytical expression of a quasi-sinusoidal signal, made up by different four sine functions is provided by the Eq 3.3:

$$y(t) = y_1 \sin \omega_1 t + y_2 \sin \omega_2 t + y_3 \sin \omega_3 t + y_4 \sin \omega_4 t \quad (3.3)$$

3.2 Concept of DOF

The number of the degree of freedom of a system is the minimum number of independent parameters that allow a full definition of the body movement in a three-dimensional space, traditionally a Cartesian system [20]. Considering this point of view, the simplest system is the one with 1 DOF, whose position in space is defined with one coordinate, and whose movement, under the action of an external force, involves the variation of this single coordinate during the time. Let now move on to consider a more complex case: a non-deformable solid body perfectly free in a (x,y,z) system. To completely describe the possible movements of its centre of gravity six quantities are required, thus it has six degrees of freedom: three for the translation movements (l_x, l_y, l_z) and three for the rotations $(\theta_1, \theta_2, \theta_3)$ around axis passing through its center of gravity. Thus the movement of each point is described through these six different quantities called generalized coordinates. The next Fig 3.3 and Fig 3.4 present two examples of simple systems with one and two degrees of freedom, of both translational and rotational type.

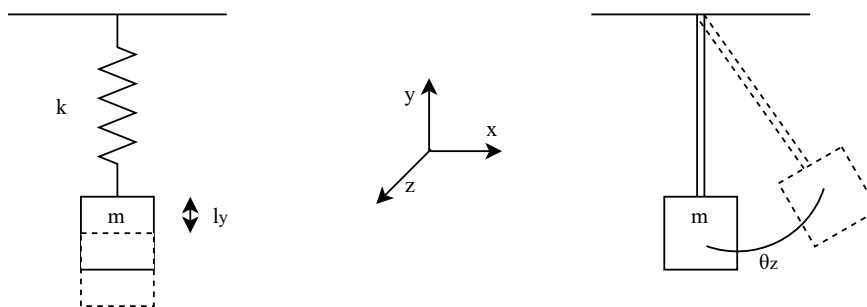


Figure 3.3: Examples of simple systems with a single degree of freedom

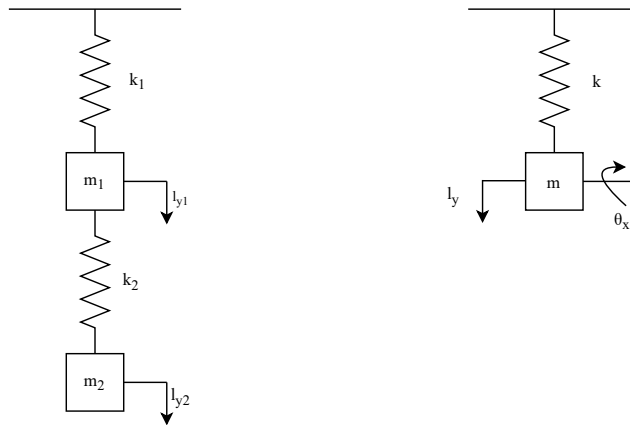


Figure 3.4: Examples of simple systems with two degrees of freedom

The aim of the following section (3.3) is to provide the basics motion equation and an explanation of the physical phenomena, regarding free damped vibration (3.3.1) and forced vibration (3.3.2), assuming as reference model the elementary system with 1 DOF.

3.3 Simple Mass-Spring-Damper Vibration Model

The vibration behaviour of many real systems can be approximated by a physical model with one degree of freedom, since only one coordinate is necessary to define the movement of the mass. This system is defined in Fig 3.5.

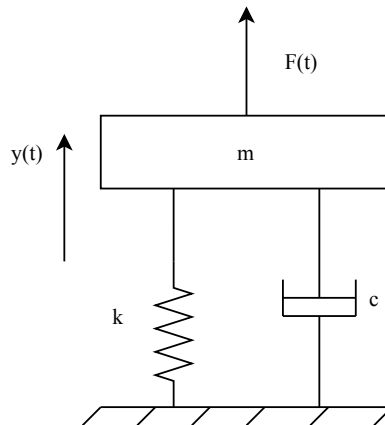


Figure 3.5: System characterized by one degree of freedom which is the output displacement $y(t)$

Thus, in particular, the fundamentals of vibration analysis can be understood by studying the schematized simple mass-spring-damper model, where $F = F(t)$ is the excitation force

and $y = y(t)$ is the displacement response, which are both functions of time, t . The constants m , c and k represent the mass, viscous damping and the spring stiffness of the system displayed in Fig 3.5:

To derive the equation of motion of this system, shown by the Eq 3.4, it is important to invoke the basic types of motion in a dynamic system, which are: the displacement y , measured from neutral position of spring and the first and second derivatives of displacement with respect to time. These derivatives are, respectively, velocity \dot{y} and acceleration \ddot{y} . Applying the Second Newton Law to the vertical direction of the system, the following balance of forces is obtained [21]:

$$m \frac{d^2 y}{dt^2} + c \frac{dy}{dt} + ky = F(t) \quad (3.4)$$

In reference to this system, it is common to express its properties through coefficients which depend from the physical parameters of the vibrating system:

$$\omega_n = \sqrt{\frac{k}{m}} \quad \text{natural frequency of the system}$$

$$c_c = 2m\sqrt{\frac{k}{m}} \quad \text{critical damping}$$

$$\zeta = \frac{c}{c_c} \quad \text{damping ratio}$$

$$\omega_d = \sqrt{1 - \zeta^2} \omega_n \quad \text{damped vibration frequency}$$

For undamped system $\omega_n = \omega_d$.

3.3.1 Free Damped Vibration

If there is no excitation, so that $F(t) = 0$, the general motion equation for this unforced damped SDOF and the general solution are provided by the Eq 3.5 and the Eq 3.6 [21].

$$m \frac{d^2 y}{dt^2} + c \frac{dy}{dt} + ky = 0 \quad (3.5)$$

$$y(t) = C_1 e^{\lambda_1 t} + C_2 e^{\lambda_2 t} \quad (3.6)$$

where C_1 and C_2 are arbitrary constants determined by the initial conditions and the eigenvalues λ_1 and λ_2 are the two distinct roots of the following characteristic equation:

$$m\lambda^2 + c\lambda + k = 0 \quad (3.7)$$

Thus, the expression of the eigenvalues is the following [21]:

$$\lambda_{1,2} = \frac{-c \pm \sqrt{c^2 - 4mk}}{2m} \quad (3.8)$$

From this formulation, it is possible to distinguish three cases from the different sign of the rooting, displayed in Fig 3.6:

Case I: $c^2 - 4mk > 0$

This is the overdamped case and the eigenvalues λ_1 and λ_2 have two different positive values, corresponding to simple exponentially decaying motion. From this case it is possible to derive the general solution of the unforced system, described in Eq 3.6 [21]

Case II: $c^2 - 4mk = 0$

This is the so called critically damped case, λ_1 and λ_2 assume the same value. It results in a simple decaying motion with at most one overshoot of the system's resting position [21]

Case III: $c^2 - 4mk < 0$

This is the underdamped case and the roots of the characteristic equation λ_1 and λ_2 are (non-real) complex-conjugates, resulting in an oscillatory motion with an exponential decay in amplitude [21].

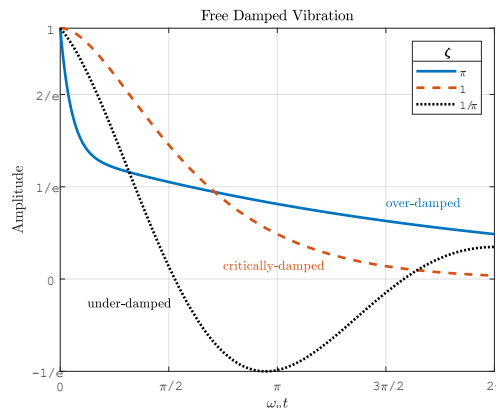


Figure 3.6: Investigation of the over-damped $\zeta > 1$, critically-damped $\zeta = 1$ and under-damped $\zeta < 1$ vibration [17]

3.3.2 Forced Vibration

When the force input is different from zero, the solution of the Eq 3.4 is expressed in the following form [21]:

$$y(t) = \left[C_1 + \frac{1}{(\lambda_1 - \lambda_2)} \Phi_1(t) \right] e^{\lambda_1 t} + \left[C_2 + \frac{1}{(\lambda_2 - \lambda_1)} \Phi_2(t) \right] e^{\lambda_2 t} \quad (3.9)$$

where Φ_1 and Φ_2 are the indefinite integrals defined by the following expressions [21]:

$$\Phi_1 = \int e^{-\lambda_1 t} \frac{F(t)}{m} dt \quad (3.10)$$

$$\Phi_2 = \int e^{-\lambda_2 t} \frac{F(t)}{m} dt \quad (3.11)$$

The constants C_1 and C_2 must be chosen to satisfy the initial conditions. Thus, if at time $t = 0$, the initial conditions are $y(0)$ and $\dot{y}(0)$ and the integrals in Eq 3.10 and in Eq 3.11 assume the value $\Phi_1(0)$ and $\Phi_2(0)$. Applying this conditions into the Eq 3.9, it is possible to find out the expression of the constants C_1 and C_2 . At this point the general solutions of the single degree of freedom system in terms of displacement, Eq 3.12 and velocity, Eq 3.13 [21] can be written:

$$y(t) = \frac{1}{(\lambda_1 - \lambda_2)} [\dot{y}(0) - \lambda_2 y(0) + \Phi_1(t) - \Phi_1(0)] e^{\lambda_1 t} + \frac{1}{(\lambda_2 - \lambda_1)} [\dot{y}(0) - \lambda_1 y(0) + \Phi_2(t) - \Phi_2(0)] e^{\lambda_2 t} \quad (3.12)$$

and

$$\dot{y}(t) = \frac{\lambda_1}{(\lambda_1 - \lambda_2)} [\dot{y}(0) - \lambda_2 y(0) + \Phi_1(t) - \Phi_1(0)] e^{\lambda_1 t} + \frac{\lambda_2}{(\lambda_2 - \lambda_1)} [\dot{y}(0) - \lambda_1 y(0) + \Phi_2(t) - \Phi_2(0)] e^{\lambda_2 t} \quad (3.13)$$

For this second case of forced vibration, the exciting force $F(t)$ acting on the system can assume different shape. It is feasible to deal with a steady-state harmonic excitation with a prescribed angular frequency or with the transient response of the SDOF system to an impulsive input force applied at time $t = 0$.

3.3.2.1 Steady-State Harmonic Response

In this first analyzed case, the exciting force $F(t)$ of the system displayed in Fig 3.5 is modeled as a harmonic force, with an angular frequency ω and a constant amplitude F_0 .

The equilibrium Eq 3.4 assumes the following form [21]:

$$m \frac{d^2 y}{dt^2} + c \frac{dy}{dt} + ky = F_0 e^{i\omega t} \quad (3.14)$$

When the starting transient time due to this force is decayed, the solution is described as a steady-state harmonic function of the following form:

$$y(t) = G(i\omega) F_0 e^{i\omega t} \quad (3.15)$$

For what concerns the exciting force of the system, in the Eq 3.14 is expressed with an exponential complex function. Considering the theory of complex number and in particular Euler's identity, it can be written in an equivalent formulation, in which both real and imaginary part is evident, taking into account that the physical solution of the problem is given only by the real part of the following complex expression:

$$F(t) = F_0 (\cos(\omega t) + i \sin(\omega t)) \quad (3.16)$$

The complex function $G(i\omega)$ is the frequency response function (FRF), also called transfer function, whose expression can be derived just replacing the Eq 3.15 in Eq 3.14 [21]:

$$G(i\omega) = \frac{1}{m(i\omega)^2 + c(i\omega) + k} \quad (3.17)$$

Taking in consideration the coefficients of the natural frequency ω_n and damping ratio ζ , with simple algebraic passages the final expression of the FRF is written in Eq 3.18 and being a complex function may be represented in terms of magnitude, as shown in Eq 3.19 and of phase, Eq 3.20 [21]

$$G(i\omega) = \frac{1}{m[(i\omega)^2 + 2\zeta\omega_n(i\omega) + (\omega_n)^2]} \quad (3.18)$$

The output/input amplitude ratio is given by:

$$|G(i\omega)| = \frac{1}{m\omega_n^2 \left[\left(2\zeta \frac{\omega}{\omega_n} \right)^2 + \left(1 - \frac{\omega^2}{\omega_n^2} \right)^2 \right]^{1/2}} \quad (3.19)$$

While the angle of phase lag φ is:

$$\tan(\varphi) = \frac{-Im\{G(i\omega)\}}{Re\{G(i\omega)\}}$$

$$\varphi = \arctan \frac{2\zeta \frac{\omega}{\omega_n}}{\left(1 - \frac{\omega^2}{\omega_n^2}\right)} \quad (3.20)$$

The Eq 3.19 and the Eq 3.20 are displayed in Fig 3.7 and in Fig 3.8. The first one shows the non-dimensional amplitude ratio $k|G(i\omega)|$ plotted against the ratio of forcing frequency to natural frequency, $\frac{\omega}{\omega_n}$, while the second shows the angle of phase θ against the same ratio of frequency. Both of them were represented for different values of critical damping ζ .

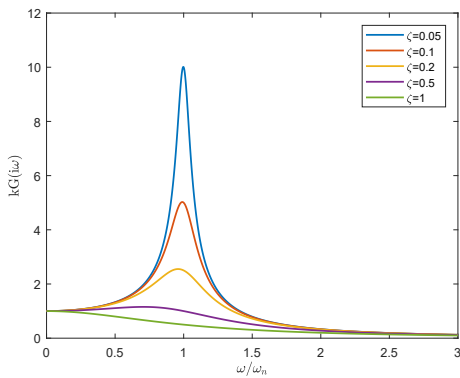


Figure 3.7: Magnitude of the frequency response function for the displacement

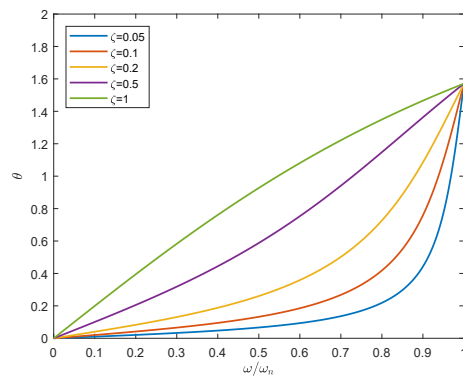


Figure 3.8: Angle of phase lag of the displacement response

The plot of these functions, called "the frequency response of the system", presents one of the most important and dangerous features in forced vibration: the resonance phenomenon. It is evident that the maximum amplitude response occurs when the ratio of the exciting frequency ω and the natural frequency ω_n is unitary, thus $\frac{\omega}{\omega_n}=1$. This effect has a huge increase with the decreasing of the damping ratio value, ζ , leading to a considerable value of magnitude. Thus, in the end, it is possible to define the resonance phenomenon, as the event that occurs in the lightly damped condition of the system, when the forcing frequency ω is near the natural frequency of the system [20]. Since this will produce the catastrophic event, due to the highly energetic phenomenon, one essential part of the vibration analysis is focused on understanding when this kind of resonance may occur and what corrective actions can be taken to avoid it. Consideration the digram plotted in Fig 3.7, it is possible to make some observations: increasing the damping ratio can lead to a mitigation of the magnitude vibration; the shift of the natural frequency of the system away from the exciting one, acting on the stiffness or the mass of the system, can also

lead to a differentiation of the frequencies under consideration. Also, changing also the property of the exciting force will provide the variation of the exciting frequency.

3.3.2.2 Impulse Response

The investigation of the response of the system under different conditions of exciting force plays an important role to accomplish the aim related to cause investigation of the broken blade. In particular, due to the strong action of the impingement system in a short period, it is worthwhile modeling the agent force on the system considering it as an impulse and analyze the general oscillatory response of the system with a single degree of freedom. In this way, the real vibration response of the blade can be evaluated as the overlap of impulse response and steady-state harmonic response. To this aim the exciting force $F(t)$ in the Eq 3.4, in the following evaluation, is considered as an impulsive input applied at $t = 0$, using the delta-function nomenclature (also called Dirac function) [21]:

$$F(t) = \delta(t)$$

This function is zero everywhere except that in correspondence of the time in which the impulse is applied, in this case for $t = 0$. In order to find the expression of the general solution Eq 3.9 the value of the integrals defined in Eq 3.10 and in Eq 3.11 need to be determined. Substituting the delta-function in the Eq 3.4 and with simple mathematical steps, the following two general expressions of the solution are derived for the different moments, before and after the application of the impulse [21]:

$$\begin{cases} y(t) = C_1 e^{\lambda_1 t} + C_2 e^{\lambda_2 t} & \text{for } t < 0 \\ y(t) = \left(C_1 + \frac{1}{m(\lambda_1 - \lambda_2)} \right) e^{\lambda_1 t} + \left(C_2 + \frac{1}{m(\lambda_2 - \lambda_1)} \right) e^{\lambda_2 t} & \text{for } t > 0 \end{cases}$$

The value of the arbitrary constant C_1, C_2 can be determined simply considering that the system is undisturbed for $t < 0$, so the response is $y(t) = 0$. In this way it is clear that the only possible value for the two constants is $C_1 = C_2 = 0$. Therefore, applying this condition and proceeding with the evaluation of the impulse response function for the two different temporal moments, the final response function $y(t)$ is expressed through the following relations [21]:

$$\begin{cases} y(t) = 0 & \text{for } t < 0 \\ y(t) = \frac{1}{m(\lambda_1 - \lambda_2)} (e^{\lambda_1 t} - e^{\lambda_2 t}) & \text{for } t > 0 \end{cases}$$

The last consideration concerning the impulse response function is about the effect of the damping ratio. As investigated in the free damped vibration, three cases are possible for the different values of damping, thus the response relative to $t > 0$, for under-damped ($\zeta < 1$), critically-damped ($\zeta = 1$) and over-damped ($\zeta > 1$), are respectively [21]:

$$y(t) = \frac{1}{m\omega_n\sqrt{1-\zeta^2}}e^{-\zeta\omega_n t} \sin\left(\omega_n\sqrt{1-\zeta^2}t\right) \quad \text{for } \zeta < 1 \quad (3.21)$$

$$y(t) = \frac{t}{m}e^{-\omega_n t} \quad \text{for } \zeta = 1 \quad (3.22)$$

$$y(t) = \frac{1}{m\omega_n\sqrt{\zeta^2-1}}e^{-\zeta\omega_n t} \sinh\left(\omega_n\sqrt{\zeta^2-1}t\right) \quad \text{for } \zeta > 1 \quad (3.23)$$

3.3.3 Multiple Degree of Freedom System

So far, all the considerations have been made for a system with one degree of freedom, however, the real vibrating systems involve more than one coordinate to specify their configuration, thus this means to have more than one degree of freedom. The number of degree of freedom is equal to the minimum number of coordinates necessary to specify the configuration of the vibrating system at any time [20].

Considering a system with N degrees of freedom, the general equation, previously obtained in Ee 3.4, maintains the same structure, however, although the constant coefficients M , c and k are matrices of order $N \times N$ and have only real elements. Thus, adopting a vector and matrix notation, the formulation of the corresponding assembled system of equations for multiple degrees of freedom system (MDOF) [21] is derived:

$$[m]\{\ddot{y}\} + [c]\{\dot{y}\} + [k]\{y\} = \{F(t)\} \quad (3.24)$$

where:

$[m]$ is the mass matrix;

$[k]$ is the stiffness matrix;

$[c]$ is the damping coefficient matrix;

$F(t)$ is the vector of the external forces;

and

$\{y\}$ is the vector of the degrees of freedom of the system of dimension $N \times 1$ and $\{\dot{y}\}$, $\{\ddot{y}\}$ are the first and second derivative, respectively.

3.3.4 Normal Modes Analysis

The purpose of this vibration investigation is the calculation of the natural frequencies of the blade.

In free vibration analysis, the number of degrees of freedom of a given model corresponds to the number of natural frequency modes that can be extracted. The equations for a free vibrating system with multiple degrees of freedom neglecting damping is [21]:

$$[M]\{\ddot{y}\} + [K]\{y\} = 0 \quad (3.25)$$

Where M and K have the structure described above. From the solution of the Eq 3.25, the natural frequency of each vibrating mode is gained. To solve this equation, for simplicity, the displacement is assumed to be represented by the following harmonic function [21]:

$$\{y\} = \{S\} \sin \omega t \quad (3.26)$$

Differentiation of the assumed harmonic solution above are:

$$\{\dot{y}\} = \omega S \cos \omega t \quad (3.27)$$

$$\{\ddot{y}\} = -\omega^2 S \sin \omega t \quad (3.28)$$

Substituting these expressions in the function of the displacement into the governing Eq 3.25, it allows:

$$-\omega^2 [m]\{S\} \sin \omega t + [k]\{S\} \sin \omega t = 0 \quad (3.29)$$

where, $\{S\}$ is the eigenvector or "mode shapes" and ω is the natural frequency of the system.

Hence, introducing some simplifications, the eigenvalue equation is given by:

$$([k] - \omega^2 [m])\{S\} = 0 \quad (3.30)$$

or in terms of generalized eigenvalues:

$$([k] - \lambda [m])\{S\} = 0 \quad (3.31)$$

Thus, the special values satisfying this equation are related to the natural frequencies by $\omega_i = \sqrt{\lambda_i}$, with the units in $\frac{rad}{s}$. The non-trivial solutions are determined imposing the following condition on the determinant:

$$\det([k] - \lambda[m]) = 0 \quad (3.32)$$

Since this is a determinant of a matrix of order $N \times N$, there will be N solutions of λ which satisfy this equation and these are the N eigenvalues, corresponding to each eigenvector or mode shape $\{S\}$ of the system.

The evaluation of the structure modal shapes is fundamental especially when a modification of its vibrating behavior directly affects the performances of the whole machine and this is perfectly aligned with this current research problem. The extrapolation of eigenvalues and eigenvectors of each vibrating mode is an expensive operation, which only for very simplified cases (at maximum 3 DOF) is possible to compute by hand. Hence an analytical solution is not feasible and it is necessary to obtain a numerical solution, using a finite element method. This computation mode and in particular, all the steps concerning the simulation are explained in the following sections.

3.4 Numerical Analysis of the Stator Blade

3.4.1 Overview of Finite Element Process

Although simple hand calculations can be very effective in the preliminary understanding of the blade behavior, more accurate results with fewer efforts are obtained with the modern computing power programs: between them, one approach followed is to perform an analysis with a Finite Element Simulator. This application is now widely used in all branches of engineering for the analysis of structures, solids, and fluids; both for static and dynamic analyses and to understand the most critical failure mechanism, such as those connected with high cycle fatigue.

The intent for which this method is used in the course of this work of thesis is to obtain the numerical solution of the mathematical problem expressed with the Eq 3.32, whose resolution will lead to the expression of eigenvalues for the vibrating system under analysis. The software used for this investigation on the stator blade is Dassault Systemes Abaqus: it is possible to use it for the creation of a part, modeling, analysis of mechanical components, assemblies, and the visualization of the results of the finite element analysis. The major advantage provided by this simulation tool is the knowledge of the natural frequencies of the blade without performing the mechanical test and their full investigation is relevant to avoid harmful resonant vibration. As detected, this consideration is significant to find out a connection between these occurrences and the happened failure.

A complete Abaqus analysis consists of three distinct stages: preprocessing, simulation, and postprocessing, displayed in Fig 3.9 and now described more in detail.

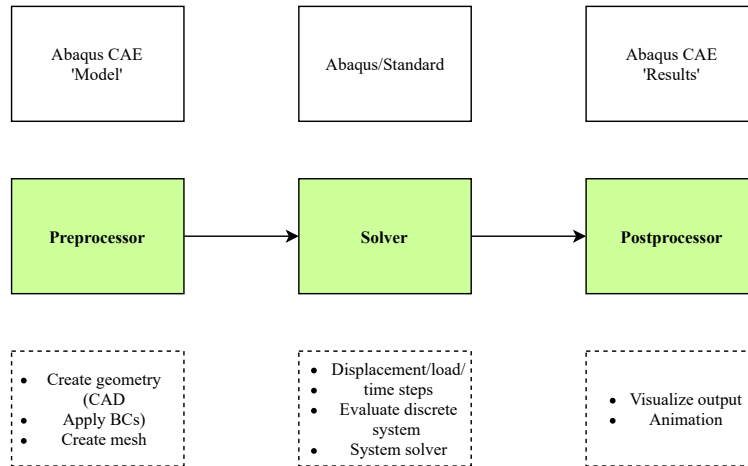


Figure 3.9: Scheme of the analysis process computed in Abaqus

A finite element analysis is performed to explore a physical problem, involving a structure or a component. The first step of the software performed evaluation is the creation of a geometric representation of the design element. The model is usually created graphically with Abaqus/CAE for simple geometry or alternately, using another preprocessor and importing the geometry. This is the start of the preprocessor phase. The created element will be referred to be the part on which the analysis is computed. If this body presents irregularities or quite complex edges, some approximations to regularize the shape can be done on the geometry, preparing the surface for the next step. Then it can be modeled to simulate real-life operational conditions, applying all the agent loads on the structure, setting the boundary condition of the real problem, and defining the material law. The core of the finite element solution, which is also the last operation of the preprocessing phase in Fig 3.9, is the meshing procedure. Its operational concept is the discretization of the complex domain into smaller and regular subdomains, using a chosen element type, known as finite elements. This implies that the real structure, having a huge number of degrees of freedom, is approximated by breaking it up into several discrete elements with a finite number of degrees of freedom. Hence, in this phase, the model of the physical problem is defined and an Abaqus input file is created [3].

The input file is submitted to the solver for the simulation. This is the stage in which Abaqus/Standard or Abaqus/ Explicit solves the numerical problem defined in the model

[3]. The output results, including, for example, displacements and stresses, are stored in binary files ready for postprocessing. Depending on the complexity of the analyzed problem and the power of the computer used, it may take anywhere from seconds to days to complete an analysis run.

Once the fundamental variables of the analysis have been calculated, the evaluation of the results occurs; so at the end of the simulation, the visualization module, reads the output file and with a variety of options, displays the results, including color contour plots, animations, deformed shape plots, and xy plots.

Since the just described finite element solution technique is a numerical procedure, it is necessary to assess the solution accuracy. If the accuracy criteria are not met, the numerical solution has to be repeated with refined solution parameters (such as finer meshes) until sufficient accuracy is reached [3].

3.4.2 Finite Element Model of the Stator Blade

The main focus of this section is to describe the performed three-dimensional finite element analysis of the blade, to determine its natural frequencies, mode shapes and through the effectiveness of the used software, a visual investigation of nodal displacement and strain. In particular, the attention is focused on the preprocessing phase, whose main steps are displayed in Fig 3.10, which leads to a discretized model of the blade, on which the simulations of the vibration field are performed.

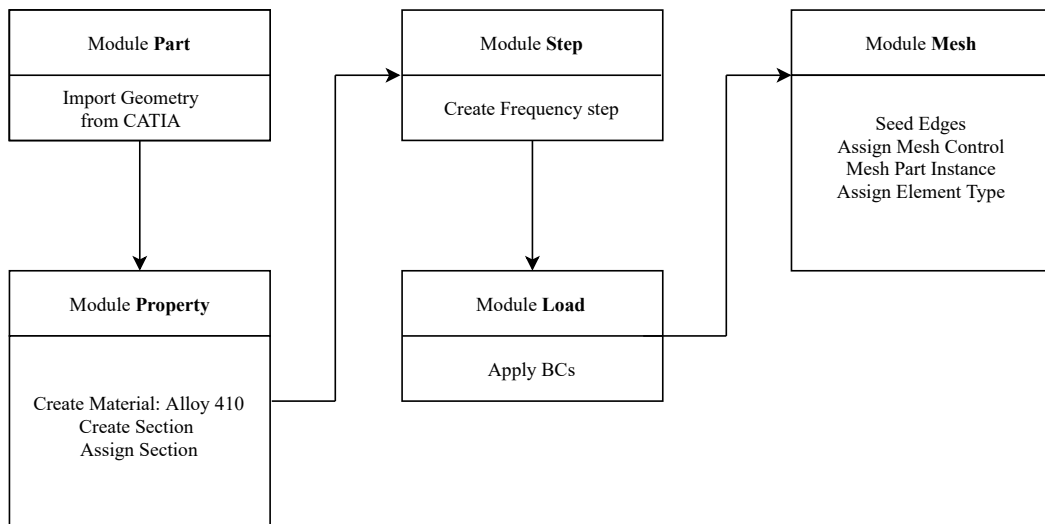


Figure 3.10: Preprocessing of the Blade Finite Model

The first module of the computed analysis is named **part**, according to Abaqus notation (see Fig 3.10). For this specific case, the model of the stator blade in exam, Fig 3.11, was previously created with CATIA V5 and imported in Abaqus as first step.



Figure 3.11: Geometry of the stator blade created with CATIA

The geometry of the blade is defined through the following dimensions, related to the figure:

- Tip chord length: 10.7 mm
- Root chord length: 12.2 mm
- Maximum thickness: 0.587 mm
- Height: 24 mm

To have a simulation of the blade behavior as close to reality as possible, it is important to take into consideration the properties of the material, that characterize the material's response to stress. They were set in the second module **property**, through the creation of the material law and of a section assigned to the blade. The material with which the blade is manufactured is the Alloy 410, a 12% chromium martensitic stainless steel, with high strength and hardness. The properties set in the creation of the material law, extracted from the datasheet, are now listed, properly converted in the International System of Units:

- Mass density: $7750 \frac{\text{kg}}{\text{m}^3}$
- Young's Module: 196 GPa
- Poisson's Ratio: 0.28

3.4.3 Lanczos Eigensolver Method for the Eigenvalue Extraction

The next module of the conducted analysis is **step**, which is one of the most relevant parts during the definition of a FE-model since analysis in Abaqus is performed using steps. In particular, the problem history is divided into steps and for each step is selected the analysis procedure, both the boundary conditions and the applied loads are defined and the output requests are specified [18]. For each step is necessary to set an analysis procedure and this choice defines the type of analysis performed during the step. To solve the eigenvalue problem (described through the Eq 3.31) for the natural frequencies extraction, only one step was created and the linear perturbation frequency procedure was set. Abaqus provides three eigenvalue extraction methods: Lanczos; automatic multi-level substructuring (AMS), an add-on analysis capability for Abaqus/Standard and subspace iteration [18]. For the analysis carried out, the Lanczos eigensolver was set and normally, it is necessary to provide the maximum frequency of interest or the number of eigenvalues required: in this case the investigation was focused on the first ten natural frequencies.

3.4.4 Mesh Refinement

As mentioned before the core of the FE-method is the creation of a grid, called mesh, whose element, named finite elements, can assume different shapes: they can be triangles or quadrilaterals for 2D-domains, tetrahedrons, and hexahedrons for 3D-domains. In this way, the continuous domain of the blade is discretized in smaller shaped elements (see Fig 3.12), where the solution of the complex problem can be approximated as a linear combination of the shape functions. The created mesh needs to properly fit the original input domain, finding the balance between a high-quality discretization, increasing with the refinement of the mesh, and the number of elements, that affects the computational efforts.

For the proper discretization of the blade geometry (Fig 3.11) first of all, it was partitioned in correspondence of geometric irregularities, which were been generated due to the importing of the CAD geometry from CATIA. Three sizes of the mesh were evaluated for the finite elements type C3D10 assigned during the simulation: it is a 10-node quadratic tetrahedron element. To determine which was the optimal size, three iteration cycles, on the partitioned new domain, have been conducted, with the following sizes of the mesh:

- Case 1: 0.50 mm;
- Case 2: 0.15 mm;

- Case 3: 0.11 mm;

As it is evident, the conducted iterations have been moved towards finer mesh, increasing the number of the employed finite elements and thus the accuracy of the solution. The final choice was to use the tetrahedrons with the global size of 0.15 mm, leading to a medium-high accuracy of the result and acceptable computational efforts. The obtained final mesh is displayed in the following picture:



Figure 3.12: Mesh adopted for the discretization of the stator blade

3.4.5 Visualization of the Results

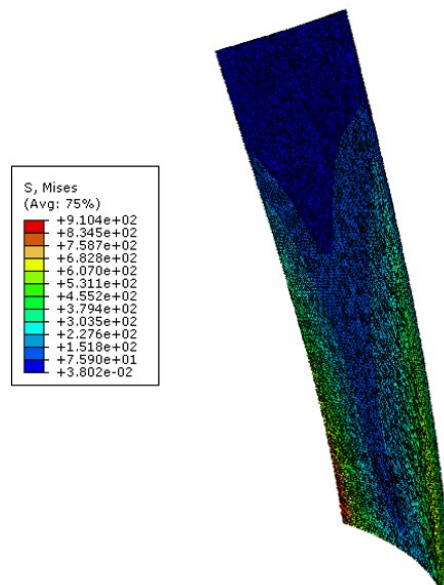
After the completion of all the modules described above, a file .input was created, it resumes the parameters of the selected analysis and all the values set: this was submitted for the evaluation. At this point, the simulation was run out into the solver Abaqus/Standard and the final stage of postprocessing was the last step, which includes the visualization and the analysis of the results.

As reported in the previous section, the investigation of the natural frequencies of the blade, with the made assumptions of neglecting the damping of the system and without any exciting force applied, was limited to the first five natural frequencies. The results in terms of frequency and of the shape motions of the blade corresponding to each value are gained running the FE-analysis with the above-mentioned conditions. For what concerns the natural frequency related to each mode, they are resumed in the following Tab 3.1.

Table 3.1: Resulting natural frequencies of the blade FE model

Mode	Natural frequency [Hz]
Mode 1	1620.4
Mode 2	4182.6
Mode 3	7404.8
Mode 4	10506
Mode 5	16784
Mode 6	18092
Mode 7	19121
Mode 8	20384
Mode 9	26887
Mode 10	28600

The shape modes connected with each frequency were displayed in the visualization module, in particular the attention was focused on the stress intensity distribution on the blade, in order to find the most stressed points, whose evaluation can be useful for the right placing of the strain gauges. The eigenmodes and the distribution of stress are illustrated in the next five images while their relative frequencies are listed in Tab 3.1. The next investigation is limited to the five natural modes.

**Figure 3.13:** First vibration mode obtained from the FE-analysis which displays the bending deformation of the blade

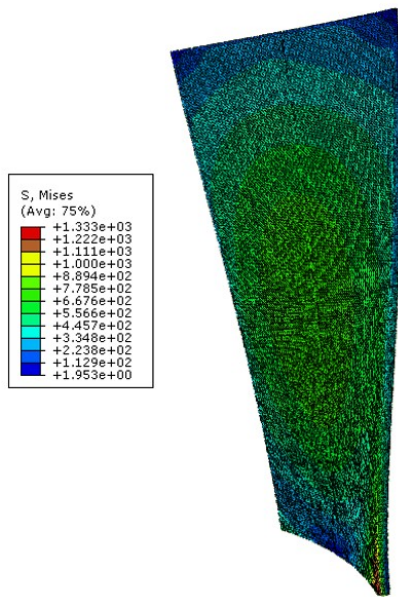


Figure 3.14: Second vibration mode obtained from the FE-analysis which displays the torsional deformation of the blade

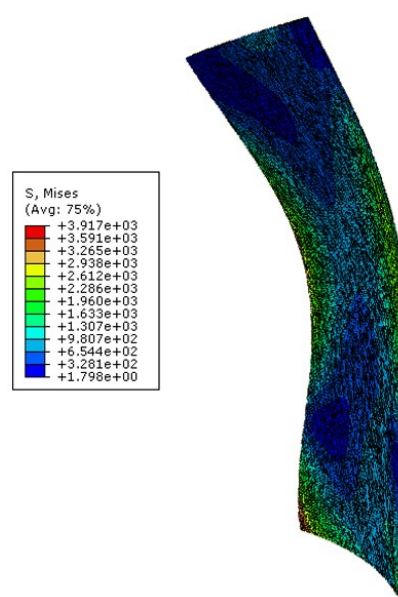


Figure 3.15: Third vibration mode which displays the coupling between the bending and torsion deformation of the blade

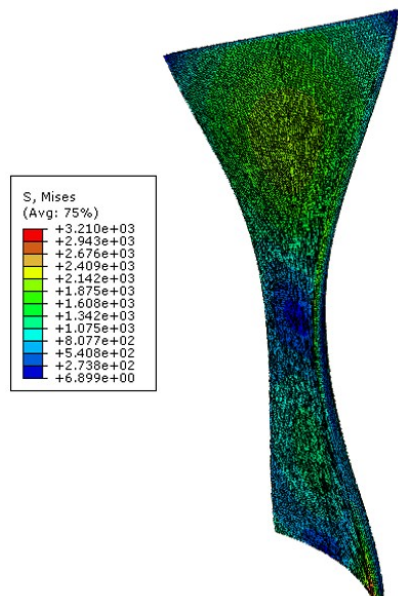


Figure 3.16: Fourth vibration mode obtained from the FE-analysis

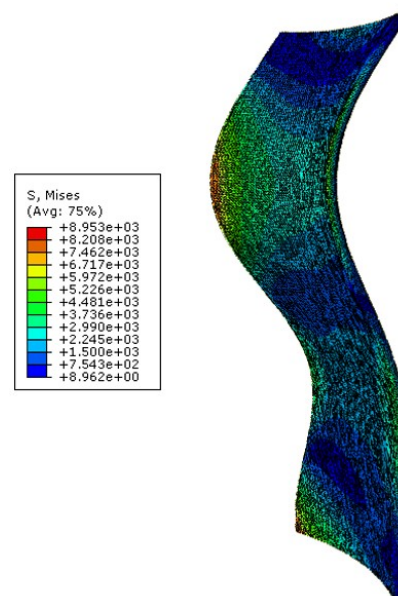


Figure 3.17: Fifth vibration mode obtained from the FE-analysis

3.5 Selection of the Strain Gauge Placement

The main task of this essay is the investigation of the vibration field born on the blade, starting from the experimental measuring of the strain, so, placing the sensor on the blade. To obtain the best results from this analysis, the measurement instruments (strain gauges) used for the testing phase, need to be placed on the blade surface taking in consideration the aim of maximize the accuracy of the gained results. Thus in this work of thesis, the right placement of sensor plays an important role in the blade modal shape investigation. It is also relevant in order to increase the quality of the signal for the subsequent step of analysis and to reduce the number of running tests effectively conducted. In this evaluation it is important to take into consideration the imposed limitation due to the small size of the blade, the sensor arrangements and the number of available sensors. With the goal to take into account and accomplish all these factors, several methods were developed, some based on intuitive consideration, some based on exact and deterministic algorithms. The approach followed during this work of investigation is the Modal Assurance Criterion (autoMac): the main purpose of this criterion is to maximize the capability to distinguish the different modal shapes and avoid misunderstanding in the definition of the modes during the experimental phase.

3.5.1 AutoMAC Criterion

This approach is based on the idea to calculate the correlation between the mode shapes, computed numerically, through the determination of the correlation matrix (Fig 3.18). The latter entails the results of the following autoMAC calculation (Eq 3.33) and was computed during the modal analysis before proceeding with instrumenting of the blade and measurement; hence, its evaluation is completely based on the vibration modes obtained with the previous described Finite-Element Simulation. The degree of correlation between the modes, displayed in the autoMAC matrix is determined with the following relation:

$$\text{autoMAC}_{i,j} = \frac{|\{\phi_i\}^T \{\phi_j\}|^2}{\left(\{\phi_i\}^T \{\phi_i\}\right) \cdot \left(\{\phi_j\}^T \{\phi_j\}\right)} \quad (3.33)$$

Where ϕ_i and ϕ_j are the eigenvectors relative to the shape modes. The dimension of the matrix is directly connected to the number of modes shown along its axes. In this specific case, the investigation analysis is focused on the first ten modes, whose eigenvectors have been acquired with the FE-analysis, thus the final dimension of the displayed MAC matrix

is 10x10. From the matrix, it is possible to see that the calculation assigns a unitary value for the modes that exactly match, along the main diagonal. The off-diagonal terms assume a value between 0 and 1, which is proportional to the degree of correlation between the involved mode shape: a value closer to 0 indicates that they are mostly unrelated, hence less probability to have interferences. In this way, all the possible combinations are compared and evaluated.

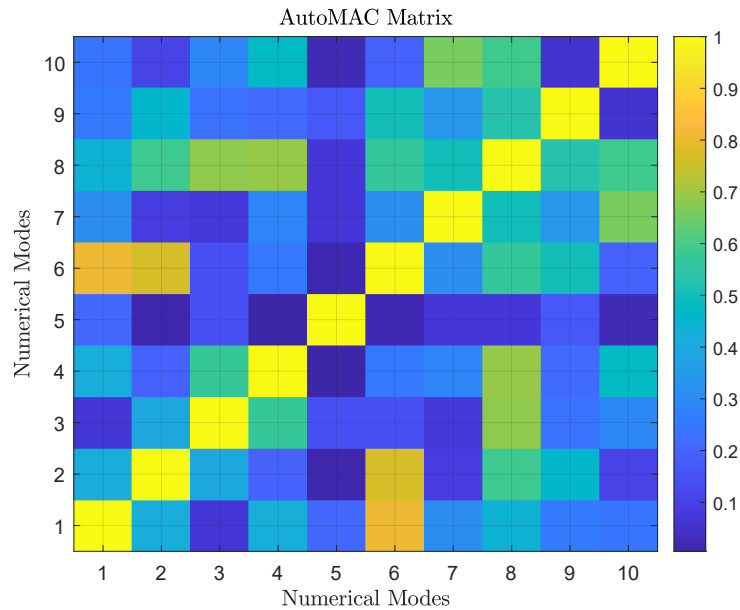


Figure 3.18: AutoMAC Matrix which displays the degree of correlation existing between the first ten natural modes

If the degree of correlation between the modes is consistent there is the concrete possibility to confuse them during the experimental investigations. However this is not so critical if the involved modes are sufficiently distant in the frequency domain; on the contrary, if they are consequent and the degree of correlation is high, this will lead to critical consequences either in their determination either in the detection of resonance phenomena. Through this analysis, it is possible to place the sensor in correspondence of most dangerous point related to the coupled modes, to increase the possibility to discern them during the experiments and establish a correct number of necessary sensors.

The calculation conducted for the modal shape of the blade under analysis has lead to the results displayed in the matrix of Fig 3.18. As evident in this case, the off-diagonal terms assume average low values, showing good chances of achieving satisfies results from the experimental analysis. The highest possibility of interference could involve the following couples of modes: Mode 1-Mode 6 / Mode 2-Mode 6, whose degree of correlation is

respectively around 0.8 and 0.9. However, although these values may appear dangerous, their frequencies are very far apart:

- Mode 1: 1620 Hz
- Mode 6: 18092 Hz
- Mode 2: 4182 Hz

Since for both the combination of modes, the risk of overlapping is estimated to be low, the decision related to the final placing of the strain gauges was taken considering the limiting space available on the blade, setting them in an intermediate position between the tip and the root of the blade, in order to have the right distance from the broken point.

Chapter 4

Methods for Vibration Measurement

4.1 Blade Vibration Measurements

To acquire and investigate the vibration of the blades during experimental tests, two stator blades have been properly instrumented, since the results from the experimental analysis are useful to understand and control the real impact of the vibrations on the blade behavior and their relation with the failure.

In order to select the most suitable detection system for the blades vibration detection an initial comparison between the existing methods, fitting the requirements of this investigation analysis, has been carried out. Among the criteria used for the evaluation have been included: the feasibility in terms of cost and accuracy; the complexity of the method; the difficulties associated with installation processes. Although all of these factors are relevant, it was also necessary to take into account the existing systems and technologies for the recording results, already available in the University laboratory. The methods analyzed during the initial comparison are the strain gauges. Below they are analyzed, and more details about their operational ways, accuracy, and feasibility are provided.

The last method involves in this initial investigation concerns the installation of the strain gauges for strain detection, which are directly placed in the point of interest. They are largely employed in sensors that detect and measure force and force-related parameters, such as torque, acceleration, pressure, and vibration. In particular, for blade vibration measurement, they represent a field-proven technology for extracting accurate real-time information relating to the strains arising in critical areas of the blade.

Two types of strain gauge exist in nature, different for their structure and properties: semiconductor strain gauges and metal foil strain gauges. Although the former ones show a higher output signal compared to the latter, they have a lot of weaknesses related to the low linearity of the output signal, meaning that the change in resistance varies nonlinearly

with strain. In addition, they show errors with high operative temperature and difficulty handling [6]. Considering these factors, the metal foil strain gauges represent the most suitable solution for the measurements, with overall high linearity between the resistance change of the gauge and the related measured strain and easy application procedures on the object.

At the end of the initial comparison phase between the methods, it was established the use of the metal foil strain gauges for the blade vibration acquisition. Although it is an intrusive and not very cutting-edge system, its applicability in a big variety of materials, its wide frequency range, and overall low-cost [6] represent strength points for using them in the subsequent experiments. Besides, the metal foil strain gauges present the great advantage of being able to install even in limited spaces and with good handling, making them suitable for the blade small dimensions.

4.1.1 Overview of Linear Elasticity

In this section, some physical principles linked with the functioning of strain gauges are provided, including some basic knowledge of the elasticity property of the material, the definition of the strain, and the linear relationship with the stress.

Elasticity is the ability of a deformable body, made up of a specific material, to resist a distorting effect and to return to its original size and shape, when the influence of force is removed [6]. If the applied force tends to stretch the material, it is called tensile force; if the applied force tends to compress the material, it is called compressive force; if it tends the shear the material, it is called shear force. Commonly, the force is defined for the unity of surface and for the compressive and tensile load is referred to be the stress, σ :

$$\sigma = \frac{F}{A} \left[\frac{N}{m^2} = \text{Pa} \right] \quad (4.1)$$

In mechanical testing and measurement, the application of an external force for the unit of surface leads to change in the spatial dimension of the body, expressed through the quantity strain, ϵ . This is the amount of deformation that the material experiences due to the application of an external tensile/compressive load. Thus, in order to operate in safety conditions, it is relevant to understand the maximum level of deformation allowed until the damage occurs. Strain ϵ , is a dimensionless quantity defined as the ratio of the change in length ΔL to the original, unaffected length L , as the following Eq 4.2 states:

$$\epsilon = \frac{\Delta L}{L} \quad (4.2)$$

The effect of a tensile force applied in both sides of the body and the subsequent strain deformation is displayed in the following Fig 4.1:

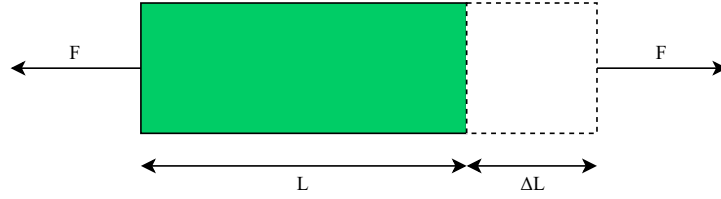


Figure 4.1: Effect of a tensile force applied in both sides of the body

From the Eq 4.2, it is evident that strain can be positive due to tensile force, $\Delta L > 0$, or negative due to compression force, $\Delta L < 0$. In the limit of the field of linear elasticity, between tensile/compressive stress and strain subsists a proportional relation, expressed with the Hooke's Law:

$$\sigma = \epsilon E \quad (4.3)$$

Where E is Young's Modulus, a property of the material, which measures the stiffness of the body under load effect. Thus, a low Young's modulus value means that the body is elastic, on the contrary, a high Young's modulus value is an indication of a stiffer body. This law exists between the value σ and ϵ and is valid only in the elastic linear field and therefore, about the curve on the plane (σ, ϵ) below the proportional limit.

If the applied force is a shear load, leading the change of the angular coordinate between two line segments, two new parameters are involved: shear strain γ and the shear stress τ . Keeping the hypothesis of remaining in the elastic field valid, between them the following relation subsists:

$$\tau = \mu \gamma \quad (4.4)$$

Where μ is the shear modulus of elasticity.

When a material is compressed in one direction, the axial direction, it tends to expand in the other directions perpendicular to the first one, called transverse. This phenomenon is described through the Poisson's coefficient, ν , a material property which is defined as the negative ratio of strain in the transverse direction to the strain in the axial direction:

$$\nu = -\frac{\epsilon_{transverse}}{\epsilon_{axial}} \quad (4.5)$$

For isotropic material, between the constants E , μ , ν the following relation subsists:

$$\mu = \frac{E}{2(1 + \nu)} \quad (4.6)$$

4.1.2 Strain Gauge: Features, Measuring Circuit and Applications

The strain gauge is a measuring device, whose electrical resistance varies proportionally with the amount of the investigated strain [6]. The following treatment is limited to the case in which this variation is linear, since, the metal foil strain gauges are more accurate than semiconductor strain gauges, as mentioned in the previous section. The following Fig 4.2 provides a representation of them, showing all the main components. The main advantages and disadvantages of this choice are now briefly resumed.

For what concerns the advantage of using metal foil strain gauges [6], the most relevant are:

- Low mass and small dimensions
- Large variety, thus specific type for each use
- Can be used for a wide selection of materials
- Wide frequency range
- Easy to handle

And the disadvantages:

- Low relative change in resistance: to solve this problem the resistances of the strain gauges are connected in a Wheatstone bridge circuit
- Limited temperature ranges
- Sensitivity against humidity, temperature, magnetic fields

Despite the different fields of application, there is a common structure for metal foil strain gauges, and the main elements of the bonded metallic strain gauge are shown in Fig 4.2.

The metallic strain gauges consist of a very fine wire or, more commonly, metallic foil arranged in a grid pattern [6]. The grid pattern maximizes the amount of metallic wire or foil subject to strain, the so-called active grid length, in the parallel direction, while the cross-sectional area of the grid is minimized to reduce the effect of shear strain and Poisson strain [6]. This grid is bonded to a thin plate, called the carrier, which is attached directly to the test specimen. Therefore, the strain experienced by the test specimen is transferred directly to the strain gauge, which reacts with a linear change in electrical resistance. Thus, the strain gauges are elements able to sense the resistance change and convert it into the

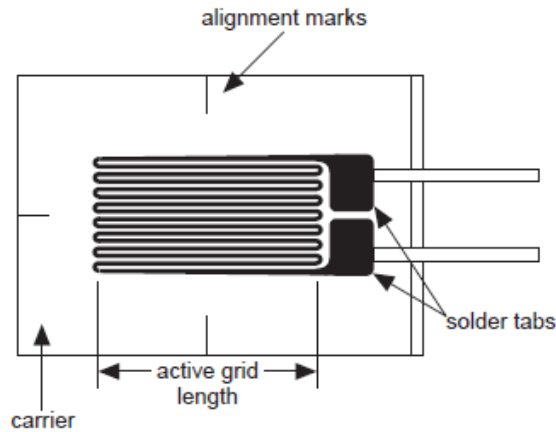


Figure 4.2: Structure and components of the metal foil strain gauge [6]

mechanical strains. A strain gauge changes the resistance of its active wire when it is stretched, or compressed. In particular, for metal foil strain gauges, resistance variation is originated through the subsequent modification of the section of the conductor, as clarified in the following relation:

$$R = \frac{\rho L}{A} \quad (4.7)$$

When the wire is subjected to a deformation that leads to stretch it (tensile load), its cross-sectional area decreases, therefore, the resistance of the strain gauge increases. The opposite happens with the compression load, with an overall decrease of the wire resistance, as shown in Fig 4.3.

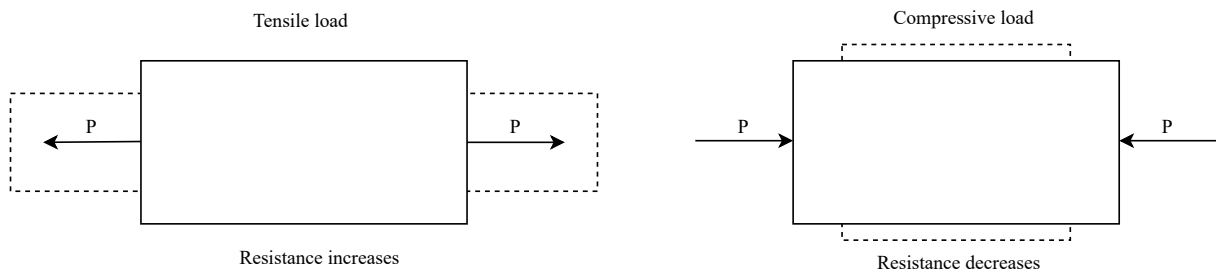


Figure 4.3: Effect of tensile/compressive load on the cross section

This change of resistance is correlated to the related strain through a non-dimensional factor, the Gauge Factor κ , according to the following proportional relation:

$$\frac{\Delta R}{R} = \kappa \epsilon \quad (4.8)$$

The most common nominal values of the resistance are: 120 Ω , 350 Ω and 700 Ω .

The gauge factor includes all the physical factors that might cause variation in the value of resistance and it is strictly affected by the temperature. Temperature can alter not only the properties of the strain gauge but also the properties of the base material to which the strain gauge is attached. Differences in expansion coefficients between the gauge and base materials may cause dimensional changes in the sensor element, therefore, additional temperature compensation is important.

The gauge factor indicates the strain sensitivity of the sensor and since it affects the measurement, the manufacturer should always supply data on the temperature sensitivity of the gauge factor. The gauge factor trend as the temperature changes, for different strain

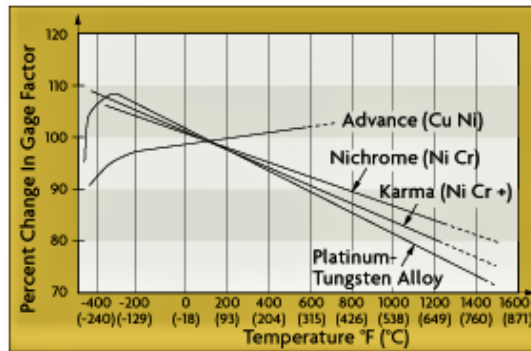


Figure 4.4: Temperature effect on the gauge factor [6]

gauge materials is illustrated in Fig 4.4. From this graph, it is evident that Copper-Nickel alloys (e.g. Advance) aren't so influenced by temperature variation and so this kind of material represents the best choice for strain gauge realization.

The strain measurements are around millistrain, therefore, very accurate instruments for measurements are required. To measure such small changes in resistance, and provide the compensation for the temperature sensitivity, the strain gauge is always used in architecture made up by four strain gauge elements electrically connected to form a Wheatstone bridge circuit, with a voltage or current excitation source (see Fig 4.5).

4.1.2.1 Strain Gauge Measurement: Wheatstone Bridge

A Wheatstone bridge is a circuit used to measure static or dynamic electrical resistance and in particular, its relevance consists in the capability of detecting relative changes of resistance in the strain gauge, which are usually around the order of $10^{-4}[\frac{\Omega}{\Omega}]$ or $10^{-2}[\frac{\Omega}{\Omega}]$, with great accuracy. The bridge circuit converts the resistance change into a voltage output and since the voltage is small as expressed in μV , it is usually amplified including an amplifier in the circuit. The following Fig 4.5 shows the basic circuit, which consists of four resistive elements located along the bridge legs; the exciting voltage is applied

between point C and A of the bridge and on the corner points B and D the output voltage is available . These elements are connected together creating the following diamond-shaped configuration:

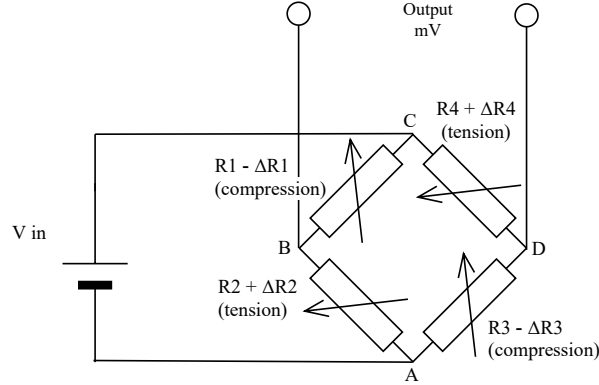


Figure 4.5: Electrical Scheme of a full Wheatstone bridge

If $\frac{R_1}{R_2} = \frac{R_3}{R_4}$ the bridge is balanced, therefore, V_{OUT} is equal to zero. For strain measurement, the resistances R_1 and R_2 must have the same value, and the same for R_3 and R_4 . A small change in the resistance of the strain gauge determines an imbalance of the bridge, thus an output voltage different from zero, making it suitable for the detection of the strain. According to the Eq (4.9), the resultant output voltage in this case, in which all the resistances are active, is directly related to the variation of the resistances in each leg of the bridge (ΔR) and the bridge excitation voltage (V_{IN}): bridge legs

$$\frac{V_{OUT}}{V_{IN}} = \frac{\Delta R_1}{R_1} - \frac{\Delta R_2}{R_2} + \frac{\Delta R_3}{R_3} - \frac{\Delta R_4}{R_4} \quad (4.9)$$

Or alternatively, considering the definition of strain expressed in Eq 4.8:

$$\frac{V_{OUT}}{V_{IN}} = \frac{\kappa}{4}(\epsilon_1 - \epsilon_2 + \epsilon_3 - \epsilon_4) \quad (4.10)$$

In the mentioned Eq 4.9 and Eq 4.10 the hypothesis that all four resistances are active is made, however, in practical applications the number of active strain gauges connected to the bridge depends from the context and from the type of deformation that is going to be investigated.

Due to the different number of active strain gauges, several configurations of the bridge exist and the most common bridge circuits are quarter bridge, half-bridge, and full-bridge, respectively with one, two, or four active strain gauges. Below a brief description of these three configurations is provided, highlighting their features and the cases of application.

- **Quarter Bridge:** One of the four resistances displayed in Fig 4.5 is replaced with an active strain gauge and any changes of this resistance from its nominal value produce an output of the bridge different from zero, to which a value of strain is connected:

$$\frac{V_{OUT}}{V_{IN}} = \frac{\kappa}{4} \epsilon_1 \quad (4.11)$$

The sign of the strain ϵ depends from compression or tension, as shown in the following figure, in which two quarter bridge are illustrated:

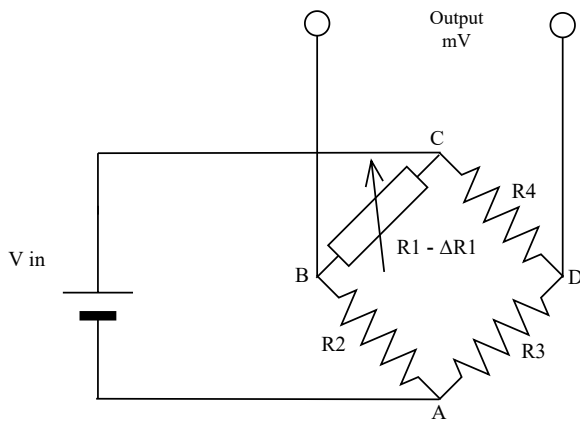


Figure 4.6: Quarter Bridge with the resistance R1 affected by tension load, leading to $\epsilon_1 < 0$

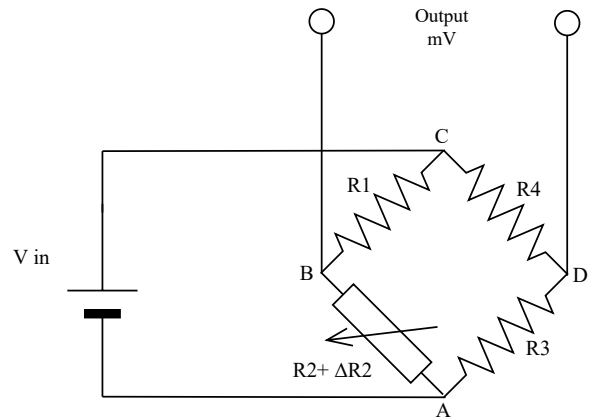


Figure 4.7: Quarter Bridge with the resistance R2 affected by compression load, leading to $\epsilon_2 > 0$

The main problem involving the quarter bridge configuration is the temperature, that affects the measurements and alters their values. To minimize the temperature change, the most commonly used solution is to have two active resistances in two different directions, leading to a double the sensitivity of the bridge. This is the configuration of the half-bridge.

- **Half Bridge:** In this case, there are two active strain gauges, as shown from the electrical scheme in Fig 4.8, with an output voltage doubled than the output of the quarter-bridge circuit and compensation of the temperature effect:

$$\frac{V_{OUT}}{V_{IN}} = \frac{k}{2} \epsilon \quad (4.12)$$

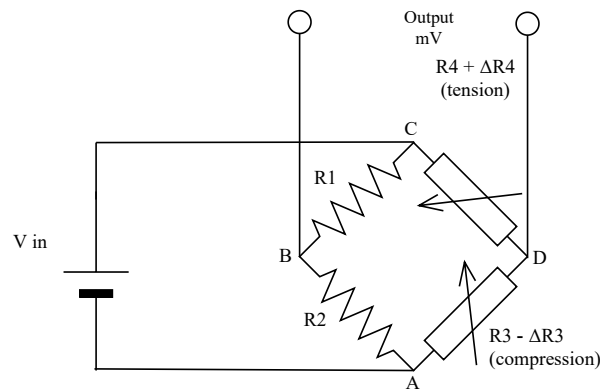


Figure 4.8: Electrical scheme of the half bridge configuration

This configuration for strain detection is widely used in the case of bending beam, shown in 4.9 in which the gauge on the upper part is in tension and bottom one in compression.

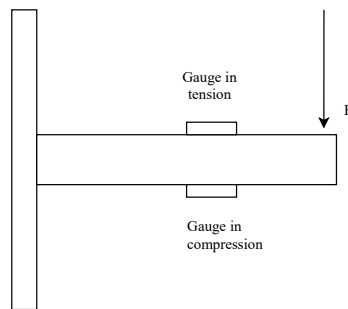


Figure 4.9: Configuration of the strain gauges for a bending beam

- **Full Bridge:** four active strain gauges.

This configuration leads to an increase of the sensitivity of the circuit and two gauges are in tension and two gauges in compression. With this arrangement it is possible to maximize the output voltage of the bridge, expressed with the following relation:

$$\frac{V_{OUT}}{V_{IN}} = k\epsilon \quad (4.13)$$

The typical configuration of the electrical circuit of the full-bridge has already shown in Fig 4.5, in which the two compressed and two stretched strain gauges are depicted.

4.1.2.2 Bridge Configuration on the Blade

To acquire the small changes of the resistances, the strain gauges are connected electrically with a Wheatstone bridge configuration. During the preliminary setting up of the test rig,

two stator blades have been instrumented with the strain gauges and connected in a half-bridge configuration to measure the strain due to the resistance changes. As previously explained, in this configuration there two active strain gauges and two compensation resistances.

The electric scheme adopted for both the bridges, including the values of active and passive resistance, and the voltage input adopted, are shown in the Fig 4.10.

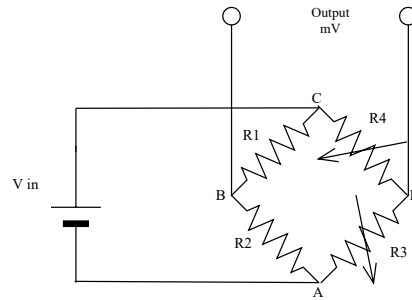


Figure 4.10: Electrical scheme of the bridge installed on the blades for the vibration measurements

- V_{in} is the input voltage of the bridge, set on 2.5 V
- $R1$ and $R2$ are the are passive resistances of value 220Ω
- $R4$ and $R5$ active strain gauges of value 350Ω and a a gauge factor equals to 2.14 ± 1 [26]
- The output voltage of the bridge is the input voltage of the connected amplifier, which has a sensitivity of 1.5001 mV/V . The output voltage of the amplifier is the value acquired by the data acquisition system through a coaxial cable

The active strain gauges have been placed on the two stator blades, in a different position, and in different orientations. In the first blade, the strain gauges have been set in proximity of the root of the blade, in a transverse position, while in the second blade along the longitudinal direction.

Chapter 5

Configuration of the Test Rig and Procedure

After preliminary numerical analysis of the blade behavior, in order to proceed with the experimental investigation of the vibration field, there was the configuration of the test rig. The existing prototype of the compressor section, developed during previous research activity [16], has been first integrated with additional parts and then instrumented with all the sensors for the acquisition of the measurements.

The three main steps of the setup phase, below described with more details, have been:

- Assembly of the compressor components
- Positioning of the measurement devices
- Establishing of the connections with display and data acquisition systems

5.1 Mechanical Integration of the Compressor Section

During the setting up phase, the experimental testbed has been assembled, including existing and new additional parts, taking advantage of the compressor's great modularity to connect multiple parts.

The installation procedures of the compressor section, have entailed the axial compressor, the impeller of the centrifugal compressor and its modified casing, on which the supply pipes, connected with the air supply of the QSS, have been installed. Since the experimental tests involve only the compressor section, without any ignition process, the integration of the diffuser, which conveys the compressed air into the combustion chamber was

not necessary.

Three new components have been integrated into the existing test rig [16], obtaining the final configuration displayed in Fig 5.1 and in Fig 5.2, employed for the following experimental tests. These pictures show two different views of the compressor section model, realized with the Software CATIA V5 and representing the starting point for the assembly operations of the experimental testbed.

Table 5.1: List of the new integrated parts into the compressor section

Nr	Component
1	Frontal Plate
2	Rear Plate
3	Impeller Ring

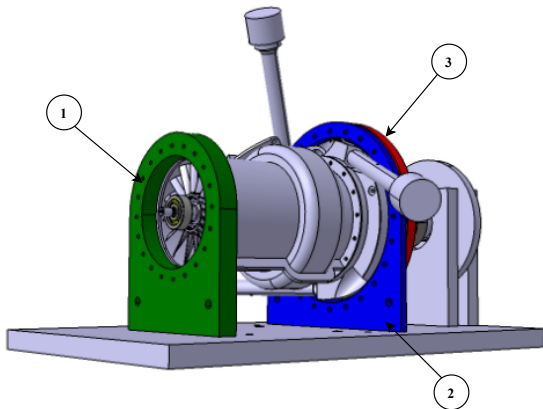


Figure 5.1: Lateral view of the integrated compressor section

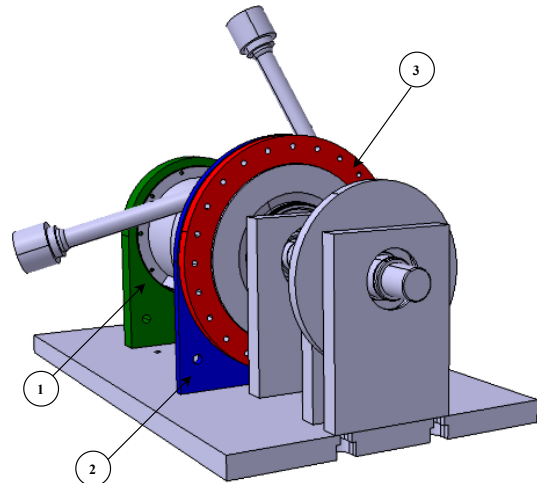


Figure 5.2: Rear view of the integrated compressor section

The frontal plate and the rear plate, listed in Tab 5.1 are depicted in green and blue in Fig 5.1 and in Fig 5.2. The first one is integrated into the inlet section of the axial compressor, while the blue one is incorporated in the impeller casing. Their bottom part is fixed on the support base, ensuring the axial alignment of all the components.

The impeller ring, highlighted in red in the above mentioned figures, is placed in the outlet section of the impeller, whose axial distance from the casing can be varied through the installation of small discs. It acts as a throttle device, which can be used to set the pressure inside the compressor during the experiments. After completing the installation

of the compressor section, the integration of the quick start system facilities was made. The air impingement system of the QSS, placed in the radial compressor casing, comprises three De Laval impingement nozzles, coupled with the relative air supply pipes. These are connected with the manifold block through three flexible rubber hoses (see Fig 2.5), which represent a suitable connection to withstand high levels of pressure.

The following Fig 5.3 displays the final configuration of the compressor section integrated with all the components, listed in Tab 5.2.

Table 5.2: List of the parts integrated into the compressor section

Nr	Component
C1	Bleed valve
C2	Compressor casing
C3	Frontal plate
C4	Rear plate
C5	Bottom plate

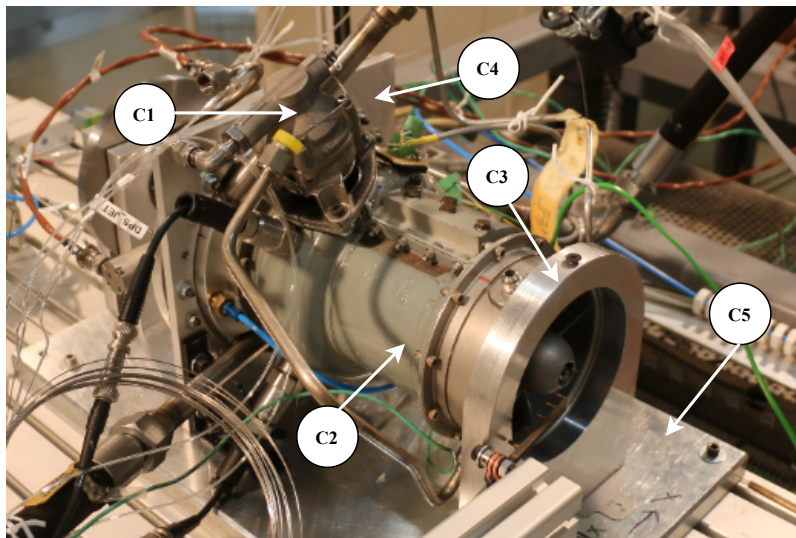
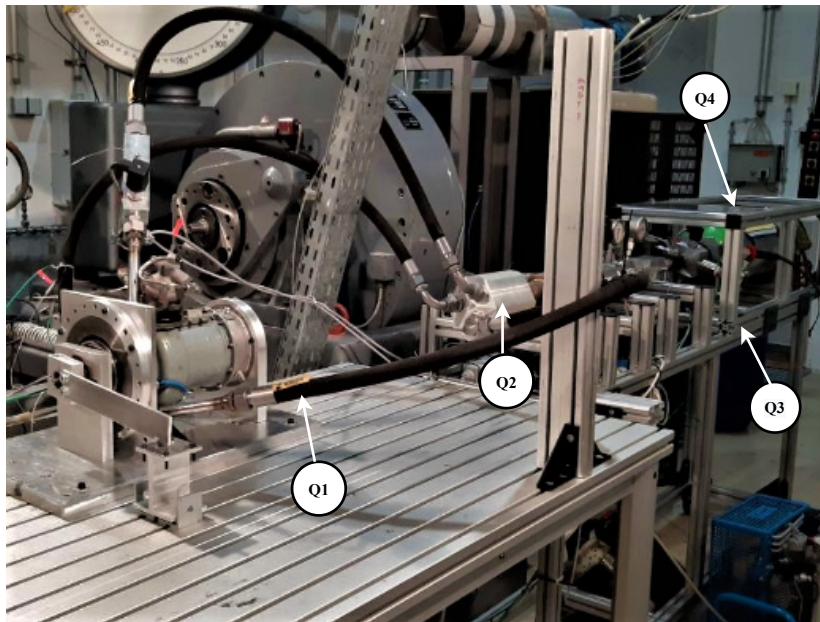


Figure 5.3: Final setup of the compressor section with all the parts and sensors integrated

The integrated final configuration of the testbed, including also the components of the air supply system of the QSS, is displayed in Fig 5.4. The components labeled are shown in Tab 5.3.

Table 5.3: List of the ASS parts integrated in the final test rig configuration

Nr	Component
Q1	Rubber Hose
Q2	Manifold Block
Q3	Bottle Rack
Q4	Compressed Air Bottle

**Figure 5.4:** Final configuration of the test rig, showing both the compressor section and the QSS

5.2 Measurement Devices

In order to acquire the measurements of the vibration field that arose due to the QSS and the related flow conditions, several types of sensors have been employed and placed in different positions. They are explained more in detail in the following sections.

5.2.1 Vibration sensors

In addition to the strain gauges installed on the stator blades four more sensors were installed during the setup of the test rig, to investigate the vibrations affecting the rear bearing and the compressor casing. To this aim, two velocity sensors for the bearing and

two accelerometers for the compressor casing were placed, whose output signals have been appropriately acquired and processed.

- **Sensor placed on the rear bearing:** The sensor installed for the measurement acquisition on the bearing is the 4-123, a vibration transducer shown in Fig 5.5, manufactured from CEC Vibration Products (CEC) [5] and suitable to work in harsh conditions. Its high-level output proportional to velocity is characterized by a low impedance and doesn't need a special amplifier. Being a self-powered sensor doesn't require an external supply voltage. All these factors lead to a simplified measurement system, making it suitable for the installation into the compressor section. The range of frequency covered by its measurement is from 45 Hz to 2000 Hz and the max peak-to-peak amplitude reached is 0.15 inch (380 mm) [5]. The analog velocity output signal is acquired from a data acquisition system and processed for subsequent analysis.



Figure 5.5: Vibration Transducer type 4–123 [5]

- **Sensor placed on the compressor casing:** For the acquisition of the vibration related to compressor casing, two industrial accelerometers IEPE sensors iCS80 were installed on the available space of the compressor casing, in the proximity of the sixth stadium, where the damaged blade has been detected. This type of sensor, displayed in Fig 5.6 and manufactured by IDS Innomic GmbH, is characterized by an insulated case and provided with double shielding for best electromagnetic interference protection, this allows it to work under rough environmental conditions. The power for its operation is provided by a DC system and the supply current is between 2 and 20 mA. The covered measurement range of this accelerometer is between ± 60

g, while the lower and upper limit of the detected frequency, are respectively 0.13 Hz and 22000 Hz [9].



Figure 5.6: Industrial Accelerometer IEPE iCS80 [9]

The sensors above mentioned were installed on the rear bearing and on the compressor casing. In the following Tab 5.4 is reported the notation used for them and the convention adopted to indicate their orientation in the local reference system of the casing and bearing.

Table 5.4: List of the vibration sensors mounted on the bearing and on the compressor casing

Symbol	Sensor location	Direction
A	Bearing	Horizontal
B	Bearing	Vertical
C	Compressor casing	Horizontal
D	Compressor casing	Vertical

Considering as reference system the base on which the compressor section is fixed, the two sensors on the bearing have been positioned along the horizontal and vertical direction, as clearly shown from Fig 5.8, while the other two on the casing have been shifted by an angle of about 45° , as schematized in Fig 5.7.

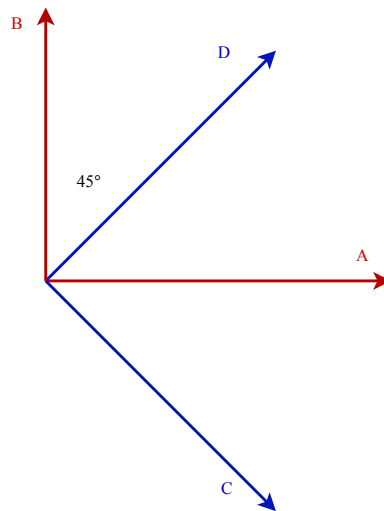


Figure 5.7: Relative orientation of the sensors placed on the rear bearing and on the compressor casing

The final integration of these vibration sensors into the compressor section, placed according to the orientation above described, is shown in Fig 5.8, where the blue color indicates the sensors installed on the casing and the red one those on the bearing, using the labels explained in Tab 5.4.

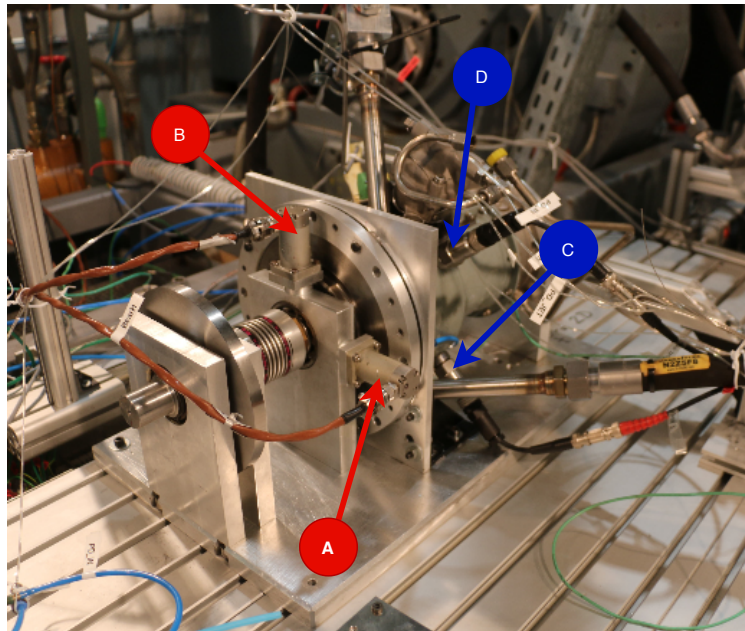


Figure 5.8: Final integration of the test rig with the installed sensors on the bearing and the compressor casing

5.2.2 Pressure Sensors

To assess the pressure values at points of interest, during the preliminary setup of the test rig some pressure sensors have been installed.

In front of the nozzle entrance of the air impingement system, two pressure sensors have been placed, for both static and total pressure, allowing the investigation of the parameters of the compressed air, before entering the nozzles. The same type of sensor was also installed to acquire the relative static pressure in the pressure regulator output. The type of sensor used for both the mentioned application is the pressure transmitter model A–10, provided by WIKA, whose measuring ranges is from 0 to 1000 bar and the non–linearity 0.25% or 0.5% [27]. For the acquisition of relative static pressure in correspondence of the impeller outlet section, the sensor Rack E1 has been used.

5.2.3 Thermocouple for Temperature Measurement

To detect the temperature in specific points of the compressor section during the experimental tests, two NiCr-NiAl thermocouples, type K, were set.

A thermocouple is made by two different metals coupled together in two electrical points. The first point is called hot junction, used for the detection of the temperature and exposed to the high temperature; the second point is called cold junction, in which the reference temperature is set. During the operations, the hot junction is exposed to a temperature different from the reference one and this leads to a gradient of temperature between the two ends. The purpose of a thermocouple is the investigation of this temperature gradient which induces an output voltage, detected by a voltage measuring device. As a result of the thermoelectric effect, or Seebeck effect, this voltage can be used to determine the temperature with the following equation:

$$V = \alpha \Delta\Theta \quad (5.1)$$

Where:

V : Measured Seebeck voltage

$\Delta\Theta$: Gradient of temperature

α : Seebeck's coefficient

The type of sensor depends on the combination of metals joined together and this influences the value of output voltage through the Seebeck coefficient, depending on the

material at the junctions.

This kind of temperature sensor has good accuracy in fast reaction time, are self-powered without requiring an external source of energy, and can be used in environments subject to harsh vibrations, however, the acquired voltage is very small, so the output signal requires amplification.

The following Fig 5.9 represents a schematization of the electric circuit employed in the K- type thermocouples used during the experiments, showing the two junctions and the voltmeter. The materials joined together are (see Fig 5.9): Chromel (90% Nickel and 10% Chromium) and Alumel (95% Nickel, 2% Manganese, 2% Aluminium and 1% Silicon) [25].

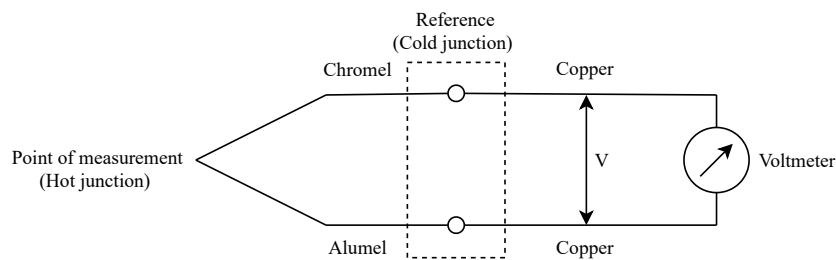


Figure 5.9: Circuit for temperature measurement with type K-thermocouple

As mentioned two thermocouples have been installed on the compressor section: one has been installed within the external casing in the proximity of the sixth axial stage, exposing the hot junction to the internal flow. The second one has been placed in front of the three nozzles, to check the temperature of the flow exiting from the impingement system.

5.2.4 Measurement of Rotational Speed

To measure the rotational speed of the compressor rotor, which is accelerated only under the effect of the quick start system a speed sensor has been mounted in the proximity of the last section of the compressor, above the impeller blades. For this aim, A PICOTURN system was used, in particular, the PICOTURN-BM V6. This is a universal speed measurement system for all standard compressor wheels and it requires a PICOTURN-BM V6 controller and a sensor, located in the measurement capture point. The controller, placed into an aluminum case, is displayed in Fig 5.10. For what concerns the sensor, it is made of a simple coil with ferrite core and placing a compressor blade in front of it, its inductance is reduced by attenuation through eddy currents [1]. This change of inductance is measured by a time-to-digital converter and the output data are processed giving a signal proportional to the rotational speed. For what concerns the controller, it has two

interfaces: the digital one, connected with the data acquisition system and the analog one, attached with the control system. The output signal of the analog interface (between 0.5 V and 4.5 V) is compared with the maximum voltage set on the control computer and when the relative speed value is reached, the rotation of the system is interrupted.

The controller is connected to a power supply system which provides it with a voltage between 8V-30V.



Figure 5.10: PICOTURN-BM V6 controller [1]

5.3 Data Acquisition System

The sensors just described, locally placed for the detection of the measurements at various points, were subsequently connected with the data acquisition systems. These systems collect the information as a voltage value, in a range between 0 and 10 V, which is converted into the relative physical value with the calibration process.

Two data acquisition systems were used due to a different range of sampling frequency required for the acquired measurements. The first one is LabVIEW, used for pressure and temperature measurements, which don't require a high value of sampling frequency. The acquisition of measurements gained from the strain gauges, the rotational speed sensor, compressor casing, and bearing vibration sensors covers higher frequencies, not covered by LabVIEW, whose maximum limit is 2500 Hz.

This necessity has led to the decision to use a second data acquisition system, IfTA ArgusOMDS (Oscillation Monitoring and Diagnostic System), a very accurate system even for high frequencies. For the sincronization of the two data acquisition systems, the coax valve signal has been used, which represents the trigger value. With regard to the data acquisition performed using the just named system, its working principle is based on a real-time oscillation monitoring and on a digital signal processor, installed in the

Argus signal process unit. This system is based on the acquisition of the analog signals through the channels installed in the Argus system with a signal processing unit. With these channels the recording of the dynamic analog signal is possible, then digitized by an appropriate A/D card [15]. If the sampling frequency of the A/D converter is lower than twice the highest frequency component, the higher frequency components, in the original analog signal, are shifted in a lower frequency within the sampled data stream [15]. This is the phenomenon of aliasing. Thus, following the Nyquist-Shannon sampling theorem, the sampling frequencies for both the data acquisition systems were properly chosen, to avoid information losses in the sampling process. For LabView was defined the value of 500 Hz, while for lftA two values were selected depending on the conducted experiments, to be able to acquire all the signals. A sampling frequency of 51.200 Hz has been used for the acquisition of blade vibrations and a value of 25.600 Hz for bearing and casing vibrations. The Argus Host application, running on the Argus Data Server, stores these data on the hard disk or provides them for the post-processing operations. The measurement system lftA ArgusOMDS is connected with the analysis software lftA TrendViewer for the visualization of the results.

As support of the operations performed before and during each experiment, there is a FADEC: it consists of a digital computer and its related accessories, that store and control all the aspects related to the status of the engine. The control algorithm, uploaded on the FADEC computer, regulates the test rig operations and includes the information regarding the value of maximum speed allowable, and the opening time of the valve, set before to conduct each experiment. The platform ControlDesk is used to display all the data concerning the engine status.

5.4 Experimental Procedure

After completing the installation and the calibration of all the sensors and of the equipment necessary to conduct the experiments, the experimental tests on the test rig have been carried out.

Before starting with the experimental tests, some preliminary steps have been necessary, including a final check of the correct installation of all components, the definition of the maximum allowed speed, and the setting of the sampling frequency for both the data acquisition systems, above described. As mentioned in the previous sections, all the investigations conducted involve only the compressor section, neglecting the combustion chamber and the contribution of the turbine on the acceleration of the compressor, narrowing the investigation only to the effect of the quick-start system, as only means to

accelerate the compressor. To this aim the compressor section and the integrated quick-start system have been tested in different operating conditions, gaining measurement of several physical variables associated with the operation.

The experiments were conducted in two main test campaigns, due to the different sensors installed. In the first campaign, the blade behavior has been investigated, evaluating its vibration response due to the QSS with the installed strain gauges. The second campaign has involved the investigation of the vibration experienced by the rear bearing and the compressor casing, acquired with the sensor above described. This procedure has led, at the end, to a broader view of the vibration effect arose on the compressor section, due to the QSS.

Both test campaigns include static tests and dynamic tests. In particular, during the static tests, the rotor was blocked with a proper instrument installed on the compressor shaft, preventing its rotation. This setup was finalized to an initial investigation of the whole system, made up of the final configuration of the test rig, thus all the equipped sensors and the QSS are included.

Later, the attention was moved on the dynamic experiments, leaving the rotor free to rotate under the acceleration effect of the quick-start system, in order to assess the contribution of rotation to the arose vibration field. For this purpose, the compressor was accelerated first until 10.000 RPM and then until 20.000 RPM.

Chapter 6

Investigation of the Results

This chapter provides the results of the conducted experiments for the stator blades, the compressor casing and the rear bearing. To this aim, each set of experiments is initially described, referring to the conditions in which it has been conducted and then analyzed more in detail by reporting the graphs of its results.

6.1 Stator Blade Experiments

The first campaign of tests has involved the investigation of the blade behavior, to analyze the vibration response and thus the effect induced by the QSS, as the main cause of damage to the blade. Since this analysis concerns the stator blades, the investigation is focused on the output measurements gained from the installed strain gauges. The half Wheatstone bridge circuit set on the involved stator blades has been previously described in section 4.1.2.2.

Before conducting the static and dynamic experiments described, respectively in Tab 6.1 and in Tab 6.2, the following common parameters have been defined:

- Relative static pressure in the pressure regulator outlet: the pressure regulator of the quick-start system regulates the level of the pressure at the entrance of the coax valve during the performed experiments. Its relevance lies in the fact that this value affects the pressure value reached in the compressor during its operation. Before carrying out the experiments in Tab 6.1 and in Tab 6.2, it was set on the value of 29 bar.
- Opening time of the coax valve: the coax valve releases the pressurized air into the nozzles during the set opening working time, thus it represents the whole range in which the impingement system works. For the set of experiments shown in this section, the value was set to 3 s.

The impeller ring integrated into the compressor section acts as a throttling device, influencing the pressure field inside the compressor and as a result also the vibration field arose in the compressor. For this reason, its relative position with respect to the impeller casing is a key point in the subsequent analyses.

For what concerns the blade static tests described in Tab 6.1 the attention has been focused on the effect connected with the position of the throttle and of the bleed valve opening. The positions of the throttle involved in this analysis are two: an opened position, meaning that the gap between the impeller casing and the rig is maximum and a closed position, where the gap is completely covered. In the following Tab 6.1 these positions are labeled with number 1 and number 2, respectively. The investigation of the most stressed points of the blade has also occurred, analyzing the results obtained by the strain gauges, positioned according to different orientations in the two blades. In one the active strain gauges have been placed along the longitudinal direction, in the other along the transverse direction.

Table 6.1: List of the conducted static tests and their characteristic parameters

Test	Throttle position	Bleed valve status	Strain gauge position
S1	1	Not installed	Longitudinal
S2	2	Not installed	Transverse
S3	2	Opened	Longitudinal
S4	2	Closed	Longitudinal

Considering the dynamic tests described in Tab 6.2 the throttle was set in position A, which is an intermediate position between the previously named position 1 and 2, respectively the opened one and the closed one.

Table 6.2: List of the conducted dynamic tests and their characteristic parameters

Test	Throttle position	Bleed valve status	Maximum rotational speed
D1	Position A	Opened	10000 RPM
D2	Position A	Opened	20000 RPM

The acquired results concern only the longitudinal strain gauge and they are not influenced by the effect of the bleed valve, since for both the experiments it has kept open. The

maximum allowed rotational speed has been set until 10000 RPM in the first experiment, D1 and increased up to 20000 RPM in the second one, D2.

6.1.1 Results from Static Tests

In this section all the graphs of the results outlined from the static and dynamic set of experiments (listed above in Tab 6.1 and Tab 6.2) are illustrated. After the acquisition, all the signals have been processed applying a sixth-order Butterworth low pass filter, to remove the noise from the original signal.

At the beginning of the analysis, the attention has been focused on the different values of the relative static pressure reached in the proximity of the impeller outlet, due to various positions of the throttle and the bleed valve. To this aim, the pressure results gained from the static test S1, S3, and S4, previously listed in Tab 6.1 have been overlapped to investigate the existing differences between the various conditions. This is summarized by the following Fig 6.1, showing that when the coax valve is opened, at $t = 0$ s, the static pressure in all the investigated tests starts quickly to grow, and at the end of a small transitory three different pressure values are reached. The lowest value corresponds to the test S1, depicted by the green line, which has been conducted with the throttle opened. Switching the throttle from opened to closed, thus minimizing the relative gap, and including the installation of the bleed valve, the red curve, concerning the test S3, shows an increase of the pressure. A further increase in the pressure level has been achieved keeping the throttle closed and closing also the bleed valve with a proper mechanism, as revealed from the blue curve, concerning the experiment S4.

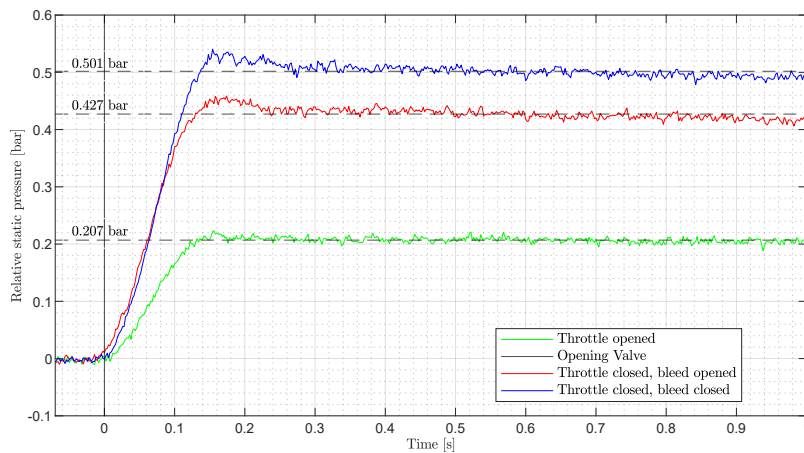


Figure 6.1: Comparison of the impeller relative static pressure reached during the static tests S1, S2 and S3

The level of pressure reached in the impeller section is directly connected with the amount of backflow, which is a portion of the $0.5 \frac{kg}{s}$ overall air mass flow entered by the nozzles of the QSS. The amount of backflow, reversed into to compressor, in the proximity of the impeller section, is correlated with the excitation of the compressor blades and their vibration field. This dependence is highlighted by Fig 6.2, which displays the different values of RMS amplitude, gained from the test S1, S3, and S4 and detected with the longitudinally placed strain gauges (Tab 6.1). The figure shows that, when at time $t = 0$ s the coax valve is switched on, there is a high increase in the RMS amplitude and after the maximum is reached, all the curves display a slight decrease. The green curve, related to the experiment conducted with the throttle opened, shows a smaller amplitude than the blue and red curves, for which the pressure level is higher, as shown in Fig 6.1.

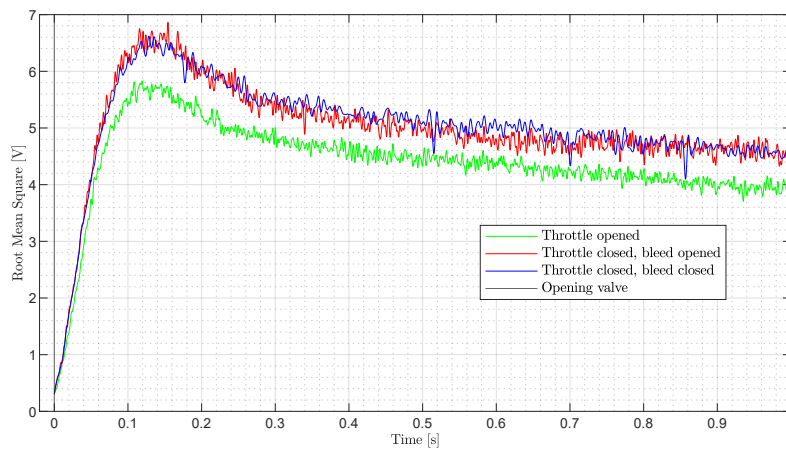


Figure 6.2: RMS comparison for the static tests S1,S3 and S4

To proceed with the evaluation of the results obtained from the static tests S1, S3 and S4 reported in Tab 6.1, a frequency domain representation of the signal has been computed. For this aim, the algorithm of Fast Fourier Transform (FFT) has been applied. This procedure has been employed to calculate the frequency spectrum of the signal gained from the static tests above mentioned and the obtained results are displayed in the following Fig 6.3, Fig 6.4 and Fig 6.5. These three graphs show an increase in the density and in the amplitude of the frequency spectrum, particularly evident in the third image.

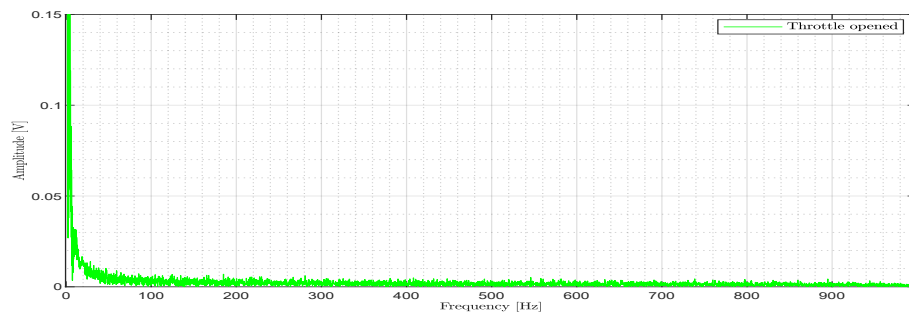


Figure 6.3: Result of the Fast Fourier Transform computed for test S1

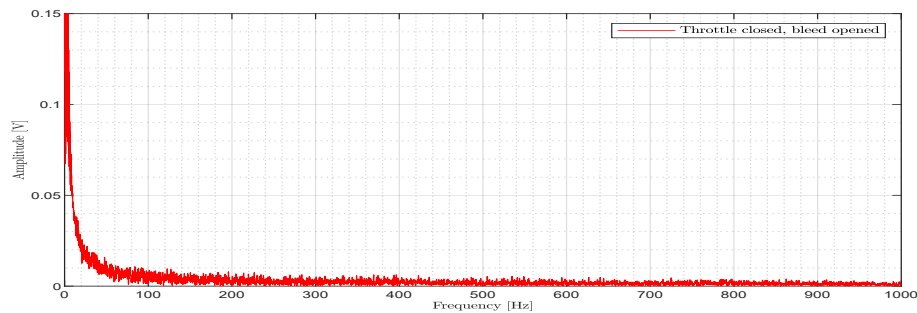


Figure 6.4: Result of the Fast Fourier Transform computed for test S3

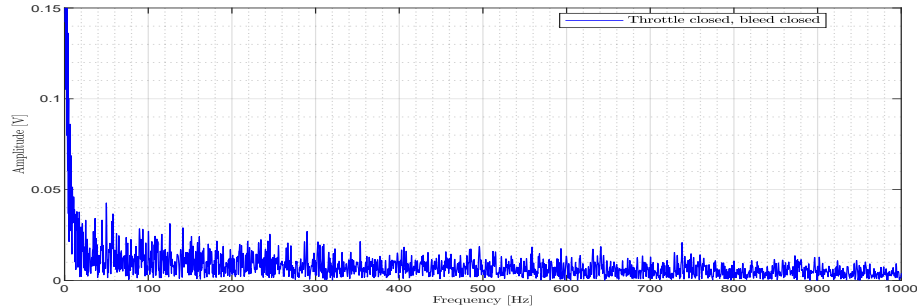


Figure 6.5: Result of the Fast Fourier Transform computed for test S4

The point that has led to the second comparison has been the evaluation of the vibration amplitude acquired by the strain gauges placed in the transverse direction and the longitudinal direction, on the instrumented stator blades. To this aim the results outlined from tests S2 and S3 listed in Tab 6.1 are overlaid in the following Fig 6.6. This graph reveals that when the coax valve is opened at 0.25 s, both the red and blue curves (relative to transverse and longitudinal strain gauges, respectively) have an increase in their amplitude, highlighting the pronounced contrast between them. The amplitude of the blue curve is higher than the red one, meaning that the longitudinal direction is much more excited than the transverse one.

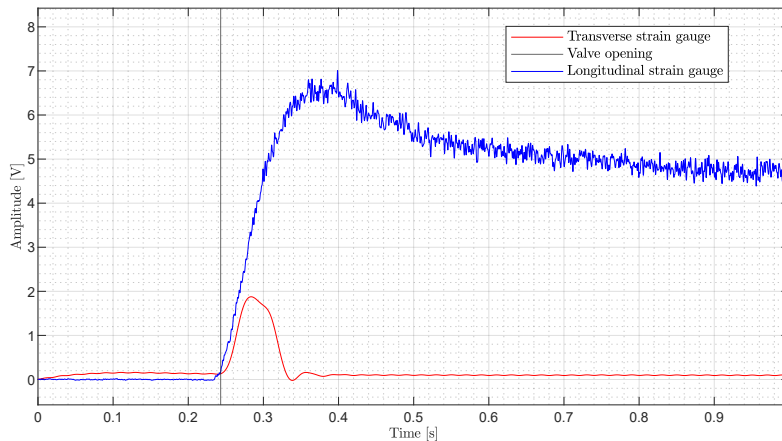


Figure 6.6: Amplitude comparison between the vibration acquired by the longitudinally and the transversely placed strain gauges

6.1.2 Results from Dynamic Tests

Proceeding with the evaluation of the blade behavior, the dynamic tests D1 and D2, listed in Tab 6.2 have been conducted. The first dynamic test has been carried out fixing the maximum achievable speed at 10000 RPM. The valve is opened at $t = 0$ s, and both the speed curve (depicted in black) and the amplitude curve (depicted in red) start to increase. The speed curve shows an increasing linear trend until the maximum speed of 10000 RPM is reached, at around $t = 1.6$ s, and at this point, the coax valve has been automatically switched off.

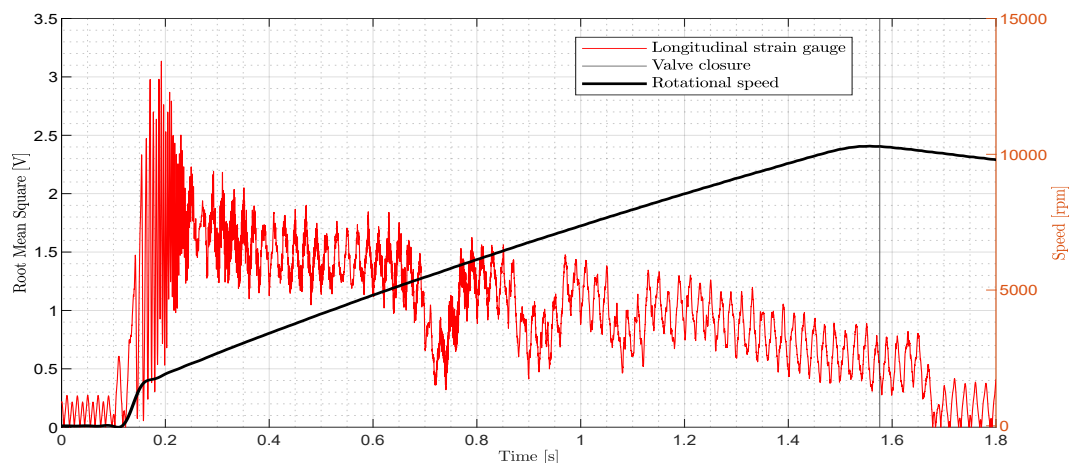


Figure 6.7: Trend of the speed curve and vibration amplitude for the dynamic test D1

To obtain the frequency range involved in the dynamic test D1 (listed in Tab 6.2), the Fast Fourier Transform has been applied to the filtered signal, leading to the following Fig

6.8, in which is evident that the dominant frequencies are localized around 2200 Hz. Also, the frequencies appearing in the lower part of the spectrum, between 100 Hz and 500 Hz, show a significant contribution.

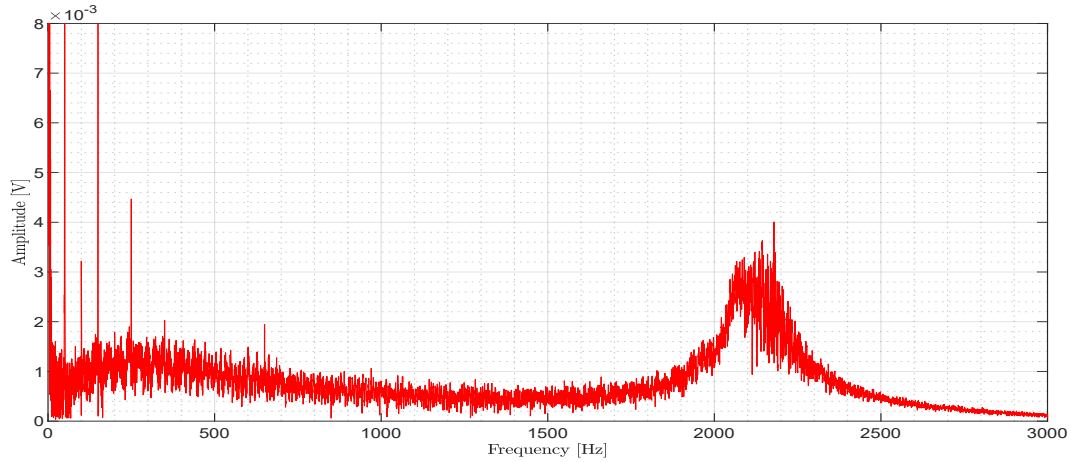


Figure 6.8: Result of the Fast Fourier Transform evaluated for the test D1

The second dynamic test D2, listed in Tab 6.2, has been conducted to investigate the blade behavior and its vibration response in more hostile working conditions, arose due to the increase of the maximum speed, set to the value of 20000 RPM. The following Fig 6.9 shows significant vibration amplitudes, whose intensity has led to an offset in the measurements acquired with the Wheatstone bridge.

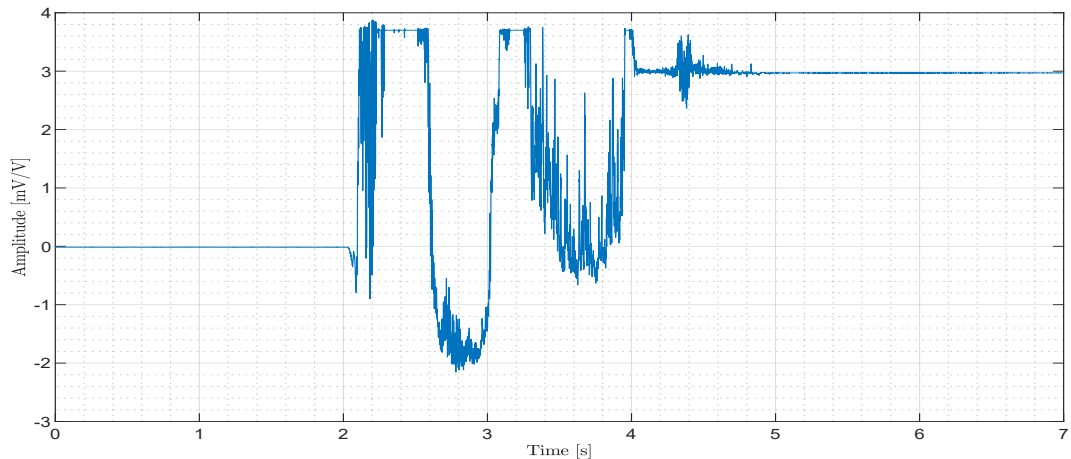


Figure 6.9: Vibration amplitude regarding dynamic text D2

For the vibration results shown by Fig 6.9 the spectrum of frequencies has also been evaluated, applying the Fast Fourier Transform algorithm, whose results are illustrated in Fig 6.10. It highlights that the frequency spectrum is more intense and with larger amplitudes at lower frequencies, in a range between 70 Hz and 200 Hz.

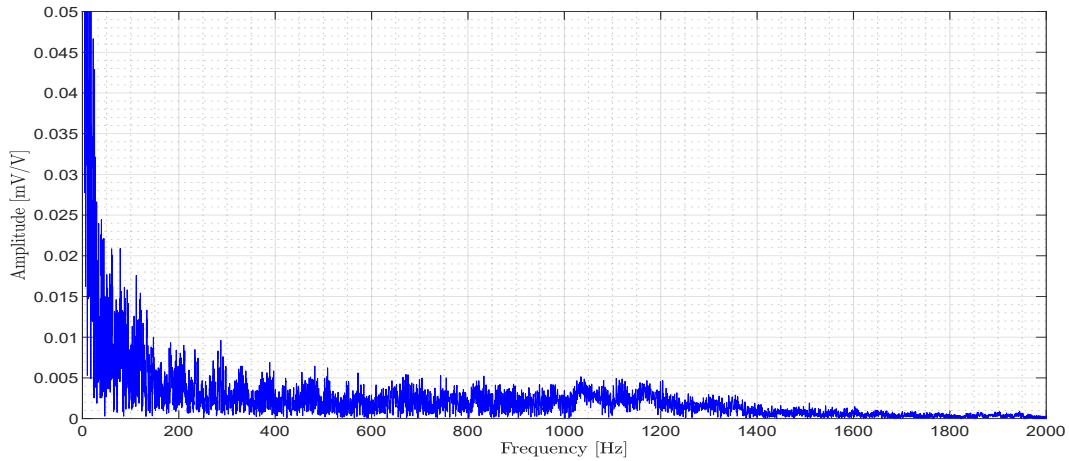


Figure 6.10: Fast Fourier Transform computed for the dynamic test D2

6.1.3 Evaluation of the Results

In this section all the results displayed in the previous section, listed in Tab 6.1 and in Tab 6.2 are evaluated and deep investigated. The examination of the results has been restricted to the interval time in which the quick-start system is working, especially in the first second after the coax valve of the QSS has been opened.

The static tests listed in Tab 6.1 have been conducted to narrow the investigation only to the effect of the QSS and to its related parameters, neglecting the influence of the rotational speed. The results displayed in Fig 6.1 and in Fig 6.2 highlight that the relative static pressure in the impeller outlet represents an influential factor in the vibration experienced by the blades. The pressure level is closely linked to the amount of back-flow which acts directly on the stator blades. Thus, increasing the pressure condition in the impeller outlet section, as displayed in Fig 6.1, the amplitude of the vibration raises accordingly, as the Fig 6.2 shows. The increasing of the pressure and therefore of the mass flow involved into the backflow, also leads to differences in the frequency spectrum, computed for the three experiments S1, S3, and S4, and shown by Fig 6.3, Fig 6.4 and Fig 6.5, respectively. The frequency spectrum computed for the experiments S1 and S3 shows only an initial peak, located at low frequencies below 100 Hz. Since there is no other factor that excites the blade, this phenomenon is linked with the vibration field originated from the QSS. This behavior is also evident in the frequency spectrum obtained for the test S4, related to higher pressure conditions. In the latter, unlike the previous ones, the frequency spectrum shows both a greater range of frequencies involved in vibrations and slightly increased amplitudes, proving how the increase in the pressure actually originates a more intense vibration field on the blades.

Continuing to analyze the results of the static tests listed in Tab 6.1, the attention is moved on the results displayed from the graph 6.6, relating to the tests S2 and S3. It shows a huge difference between the amplitude of the vibration acquired by the transversely placed strain gauges and the longitudinal ones. The vibrational modes of the blade have been provided through the investigation of the results outlined from the finite element simulation, whose results are reported from Fig 3.13 to Fig 3.17, in particular in Fig 3.13 the bending mode of the blade is evident, while in Fig 3.14 and in Fig 3.16 the torsional mode is highlighted. Considering these results, the transverse strain gauges have been placed in proximity of the root of the blade, in order to investigate the torsional mode and a possible coupling between twisting mode and bending mode of the blade. Differently, the position and orientation of the longitudinally placed strain gauges make them suitable for the investigation of the bending deformation mode of the blade. The results shown by Fig 6.6 reveal that the longitudinal direction of the blade is more excited, since the relative curve, depicted in blue, has a higher amplitude in comparison with the red one, relative to the transverse direction. Both the experiments involved in this analysis (S2 and S3 described in Tab 6.1) prove the existence of a vibration field on the blade, although characterized by a different intensity, showing that the primary shape deformation mode of the blade is the bending mode (Fig 3.13).

To analyze the effect of the rotational speed into the vibration field that arose on the blade, the focus is now moved on the investigation of the results obtained from the tests D1 and D2. The acceleration of the rotor was obtained through the airflow entered by the nozzles, which were placed to provide the maximum effect on the acceleration, as previously described in section 2.2.1. During the dynamic test the resulting vibrations are a combination of both the vibration originated from the impingement system, and of the effect linked with the rotor dynamics. This is evident comparing the results of the Fast Fourier Transform shown by Fig 6.5 for the static test S4 and by Fig 6.8 for the dynamic test D1. The graph for the dynamic experiment, depicted in red, shows two spikes, meaning that these frequencies have much stronger intensities than the others. The lowest spike is localized at low-frequency, around 250 Hz, while the highest around 2200 Hz. The frequency spectrum shown in Fig 6.5, for the static test S4 doesn't highlight such frequency spikes. This leads to the conclusion that the vibration field generated by the rotational speed emphasizes the low vibration frequencies associated with the QSS and originates a vibration field with higher frequency, localized around 2200 Hz. By increasing the speed up to 20000 RPM, the resulting vibration field related to the dynamic test D2 and reported in Fig 6.9, shows an offset in the output voltage of the bridge the blue curve

is set on the value of $3 \frac{mV}{V}$ when the coax valve is switched off, after 4 s. This value different from zero is the result of a residual deformation involving the active resistance acquired by the Wheatstone bridge even when the QSS is deactivated.

6.2 Compressor Section Experiments

The second test campaign conducted during the experimental investigations has involved the analysis of vibration experienced by the compressor casing and the rear bearing, due to the QSS action. The sensors used to acquire the results and their positioning have been shown previously in Fig 5.8. The results obtained from these experiments, in addition to those concerning the blades, allow gaining a broader view, regarding the vibration field that arose on the compressor section due to the QSS. During this campaign, some tests were conducted with the rotor blocked, and others with the rotor accelerated up to the maximum speed of 20000 RPM, through the QSS. The position of the impeller ring, acting as throttling device has been fixed in an intermediate position, between open and closed, labeled with the letter A in Tab 6.3. During all the conducted experiments this position was maintained unchanged and only the pressure value established in the pressure regulator was modified. This has led to different conditions of vibration, investigated in more detail in the next sections. As displayed from Fig 2.5 the pressure regulator of the QSS is connected with a release ball valve, through which the pressure value was set manually before each experiment. Since the pressure level in front of the pressure regulator changes, the air mass flow through it is also affected, involving also the total pressure in the nozzle supply pipe and the amount of backflow. The opening time of the coax valve was set for all experiments equal to 4 s.

The following tests, listed in Tab 6.3 and in Tab 6.4, have been conducted.

Table 6.3: List of the static tests conducted for the evaluation of the vibration on the compressor casing and rear bearing

Test	Throttle position	Pressure set of pressure regulator
S001	Position A	32 bar
S002	Position A	27 bar
S003	Position A	40 bar

Table 6.4: List of the dynamic tests conducted for the evaluation of the vibration on the compressor casing and rear bearing

Test	Throttle position	Pressure set of pressure regulator	Rotational speed
D001	Position A	32 bar	20000 RPM
D002	Position A	27 bar	20000 RPM
D003	Position A	40 bar	20000 RPM

6.2.1 Results Reporting

In this section all the results gained from the conducted experiments listed in Tab 6.3 and in Tab 6.4, are shown. The results displayed in this section have been acquired by the respective acquisition systems and later processed, using a proper filter. The following filter types have been applied:

- Bandpass Butterworth filter: this kind of filter designed to have as flat a frequency response as possible in the passband, was set on the low cutoff frequency of 100 Hz and on the high cutoff frequency of 3000 Hz. It has been employed for the processing of signals acquired from the casing accelerometers.
- Low pass Butterworth filter: the measurement data acquired by the pressure sensors and from the rear bearing sensors, have been filtered using a sixth-order low pass filter, with the cutoff frequency set on 3000 Hz.

The first set of the reported results concerns the dynamic test D001, carried out according to the conditions listed in the Tab 6.4. The vibration field arose into the compressor casing, in term of RMS amplitude are shown in Fig 6.11. In this graph also the trend of the rotational speed is represented. When the coax valve is switched on, at $t = 0$ s, the red curve and the blue one, concerning the sensors positioned horizontally and vertically, respectively, show both a huge increase. Their trend along the time follows the increase of the rotational speed until the maximum is reached and the valve is closed at $t = 4$ s. From this point on, although there are still peaks in the amplitude values, both the curves tend to decrease.

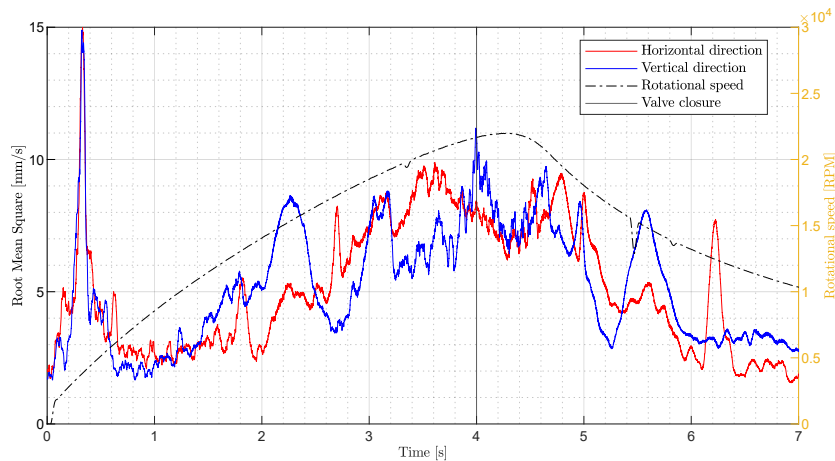


Figure 6.11: Compressor casing vibration acquired by the horizontal and the vertical sensors during the dynamic test D001

The vibration field experienced from the rear bearing during the same experiment is different and its trend is shown in Fig 6.12. Both the red and blue curves show an increasing trend, closely linked to the trend of rotational speed, and the vibration amplitude acquired by the horizontally placed sensor, depicted in red, is much higher.

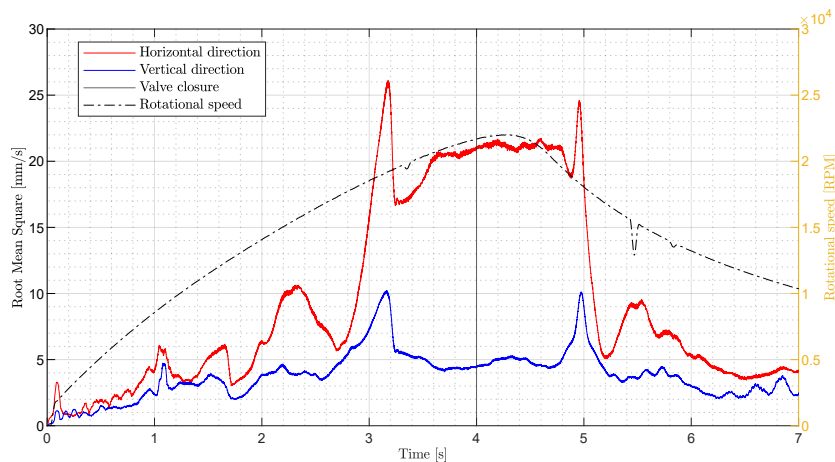


Figure 6.12: Rear bearing vibration acquired by the horizontal and the vertical sensors during the dynamic test D001

To evaluate the spectrum of frequencies, concerning the vibration of the compressor casing and the rear bearing, the Fast Fourier Transform of the data has been computed. The outlined results for the compressor casing are depicted in Fig 6.13 and in Fig 6.14.

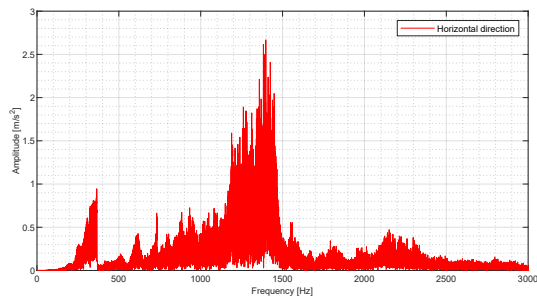


Figure 6.13: Fast Fourier Transform computed for the vibration acquired by the horizontal sensor placed on the compressor casing

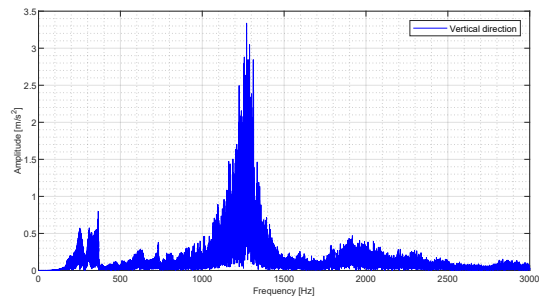


Figure 6.14: Fast Fourier Transform computed for the vibration acquired by the vertical sensor placed on the compressor casing

The frequency spectrum computed for the vibration experienced by the rear bearing has led to the results displayed in Fig 6.15 and in Fig 6.16, for the horizontal and vertical direction of the sensor, respectively. Both of them show an intense peak localized around 400 Hz, while only the second spectrum depicted in blue, shows some amplitude peaks even for higher frequencies.

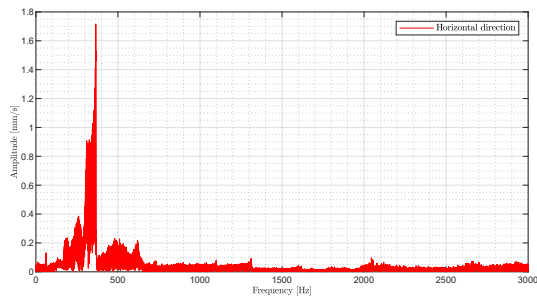


Figure 6.15: Fast Fourier Transform computed for the vibration acquired by the horizontal sensor placed on the rear bearing

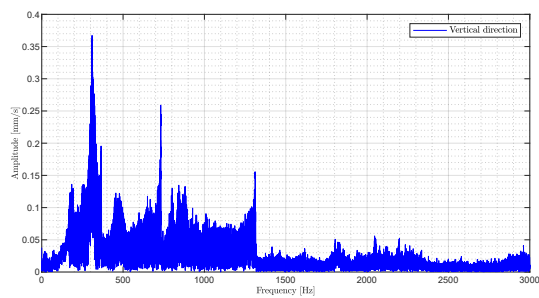


Figure 6.16: Fast Fourier Transform computed for the vibration acquired by the vertical sensor placed on the rear bearing

To investigate and distinguish the effects originated from the QSS and the rotor dynamics, the results gained from the dynamic test D001, just analyzed, have been overlaid with the results related to the static test S001, mentioned in Tab 6.3.

Both these tests have been conducted with the same pressure value set in the pressure regulator, however, the relative static pressure reached in the impeller outlet section is different, as shown from Fig 6.17. Both green and red curves start to increase when the coax valve is opened, at $t = 0$ s, but when the transitory is ended, the red curve of the dynamic test reaches a higher value of pressure, due to the contribution provided by the operation of the compressor.

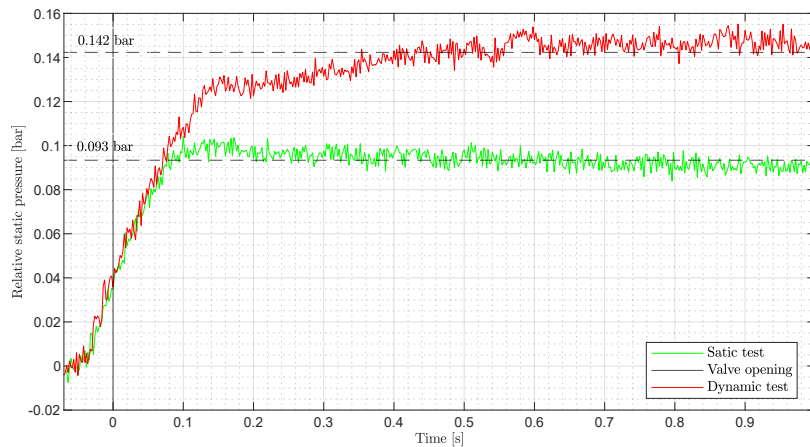


Figure 6.17: Relative static pressure reached in the impeller outlet section during the static test S001 and the dynamic test D001

Also, the vibration field experienced by the compressor casing, whose investigation is restricted to the results acquired from the sensor positioned in a vertical direction, is severely affected by the rotation of the rotor, as Fig 6.18 shows. The red curve displays a much more amplitude during the time, with an initial peak as soon as the valve is opened, which is not present in the green curve, relative to the static test.

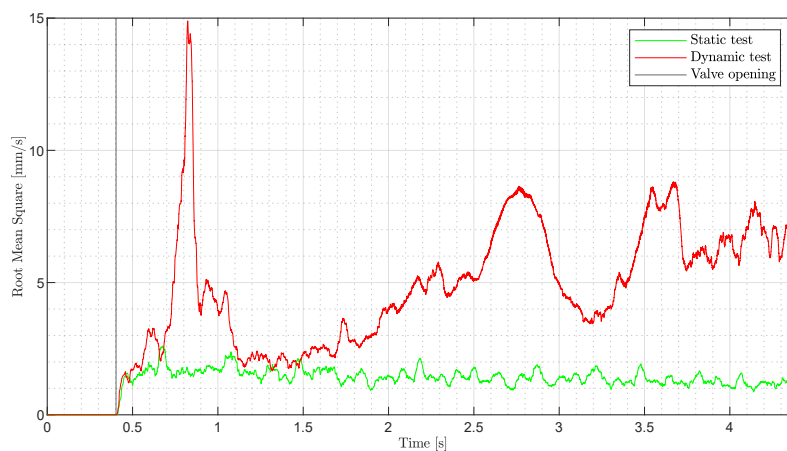


Figure 6.18: Vibration amplitude comparison between the static test S001 and the dynamic test D001

The computed Fast Fourier Transform of these vibration signals, displayed in Fig 6.19 and in Fig 6.20, show in both that the main frequency of the signal is localized at around 1400 Hz, with a higher intensity for the red curve, relative to the dynamic test D001. The latter also shows a low-frequency component in the spectrum, not present in the green spectrum, the cause of which may lie in the vibration field arose due to the acceleration of the rotor.

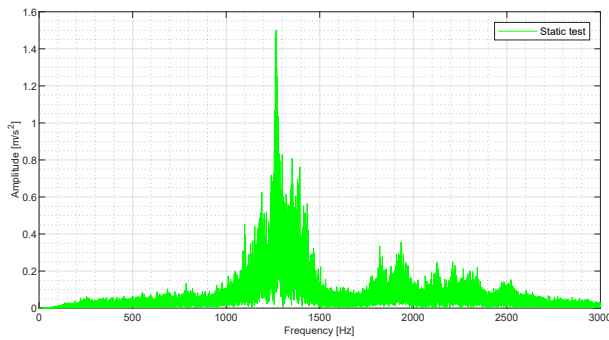


Figure 6.19: Fast Fourier Transform computed for the static test S001

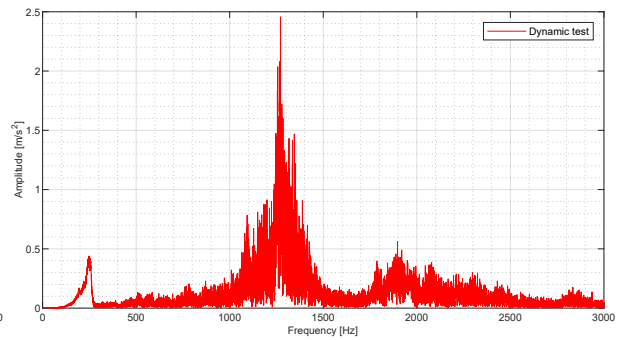


Figure 6.20: Fast Fourier Transform computed for the dynamic test D001

To assess the effect of the increase of the pressure in the pressure regulator, the result gained the static tests S001, S002, and S003, listed in Tab 6.3 are compared and evaluated through the following graphs.

The first effect associated with the increase of the pressure set in the pressure regulator is the consequent rise of the relative static pressure in the impeller outlet, as displayed from Fig 6.21. All three curves start to grow when the coaxial valve is opened at $t = 0$ s, and at the end of the initial transient, they reach three different pressure values directly linked to the pressure value defined in the pressure regulator.

The pressure increase leads to the raise of the amplitudes of the vibration experienced by the compressor casing, as revealed from Fig 6.22, thus the red curve shows the higher amplitude since it is associated with the greatest pressure value set in the pressure regulator.

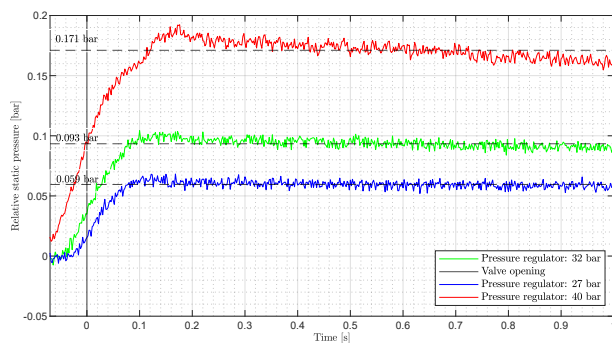


Figure 6.21: Comparison of the reached impeller static pressure during the static tests S001, S002 and S003

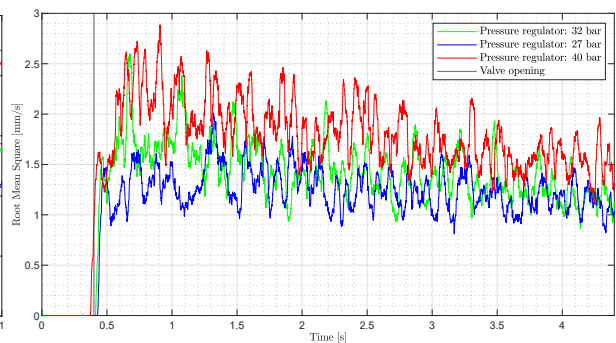


Figure 6.22: Comparison of the vibration amplitude affected the compressor casing during the static tests S001, S002 and S003

The Fast Fourier Transform computed for the static tests S001, S002 and S003, listed in Tab 6.3, to evaluate their spectrum frequency, are displayed in Fig 6.23, in Fig 6.24 and in Fig 6.25. For all of them, the most relevant frequency of the signal is around 1400 Hz.

The amplitude of this peak shows a slight increase with the rise of the pressure value set in the pressure regulator, phenomenon visible comparing the following green, blue, and red spectrum.

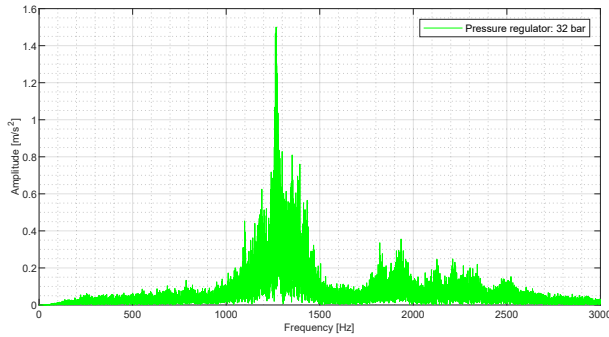


Figure 6.23: Fast Fourier Transform computed for the static test S001

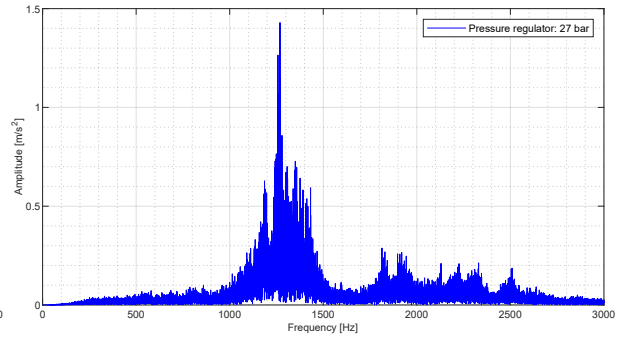


Figure 6.24: Fast Fourier Transform computed for the static test S002

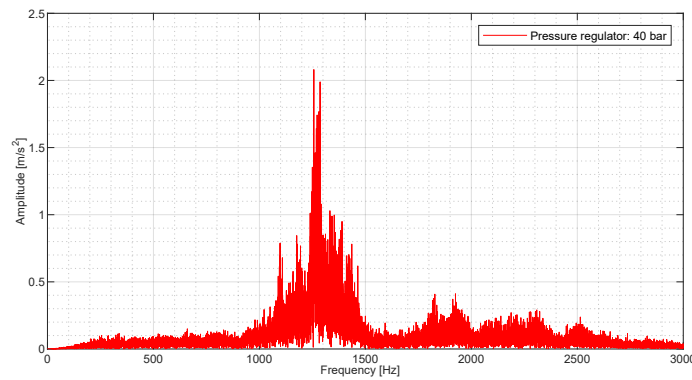


Figure 6.25: Fast Fourier Transform computed for the static test S003

The last investigation involves the analysis of the effect due the increase of the pressure set in the pressure regulator for the dynamic tests D002 and D003, listed in Tab 6.4. To this aim the graph showing the vibration amplitude of the compressor casing for both the experiments is obtained in Fig 6.26.

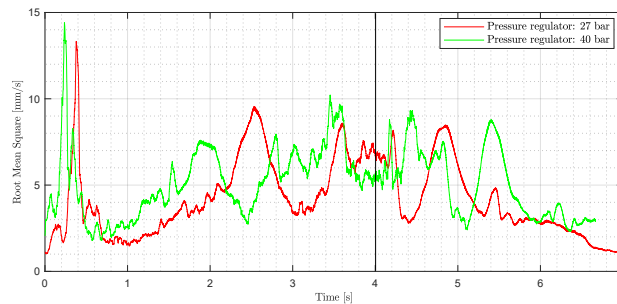


Figure 6.26: Comparison between the vibration amplitude of the casing for the dynamic tests D002 and D003

To have a complete view, the spectrums of the frequencies related to these experiments have been computed, portrayed in red and green respectively in the following Fig 6.27 and Fig 6.28.

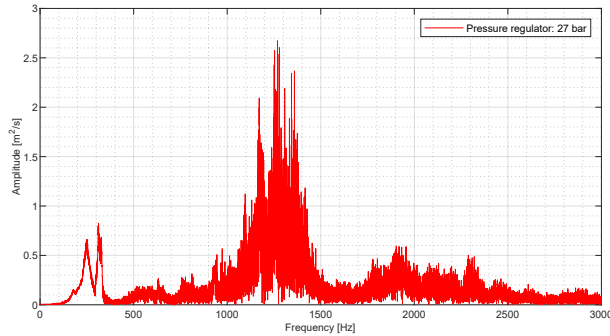


Figure 6.27: Fast Fourier Transform computed for the dynamic test D002

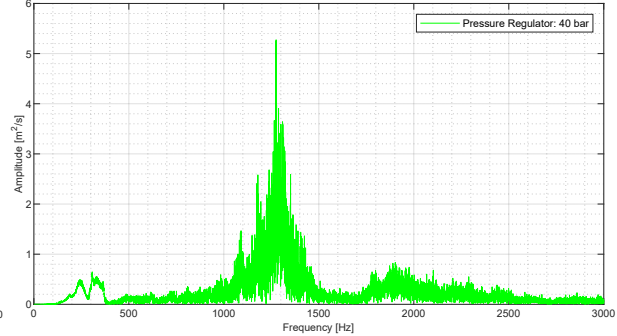


Figure 6.28: Fast Fourier Transform computed for the dynamic test D003

6.2.2 Evaluation of the Results

During the dynamic test D001, both the compressor casing and the rear bearing are affected by a conspicuous field of vibration, as Fig 6.11 and Fig 6.12 display. The vibrations experienced from the compressor casing have almost the same intensity and the same trend in both horizontal and vertical directions. On the contrary, the vibration field that arose on the rear bearing is more intense along the horizontal direction than in the vertical one, as shown in Fig 6.12. This difference may be attributed to the position where the vertically placed sensor has been installed. As Fig 5.8 displays, this vibration sensor identified with the letter B, has been installed on a plate constrained in the bottom part, for this reason, the vibrations acquired are more damped than those gained by the horizontally placed sensor.

In addition, the vibration field which involves the rear bearing, displayed in Fig 6.12, shows a rather symmetric trend before and after the closure of the valve. When the coaxial valve of the QSS is closed, at $t = 4$ s, the vibrations that exist due to the rotational dynamics of the rotor, show some spikes with a smaller amplitude than those that appear specularly in the working range of the QSS. Comparing the frequency spectrums computed through the FFT algorithm, for both the compressor casing (Fig 6.13 and Fig 6.14) and the rear bearing (Fig 6.15 and Fig 6.16) the most relevant vibration frequencies are highlighted. For the compressor casing the higher component is around 1400 Hz, while for the rear bearing is 300 Hz. This frequency peak localized at around 300 Hz is connected with the vibration phenomena arose during the rotor acceleration, since it appears only into the frequency spectrum of the dynamic tests. Looking at the frequency spectrum of the static

test S001, shown in Fig 6.23 this frequency is not evident, and it shows that the main frequency of the signal is 1400 Hz. These observations lead to the conclusion that the recurring peak at the frequency of 1400 Hz in the vibration spectrum computed for the casing of the compressor, is due to the vibration field originating from the QSS since it appears for both static and dynamic tests. By evaluating the vibration trend shown through the graph in Fig 6.18, is evident that the rotor acceleration affects not only the frequency spectrum but also the amplitude of vibrations. In particular, the red curve related to the dynamic test D001 shows a huge peak at the beginning, not appearing in the green curve of the static test S001. Since this peak occurs immediately after the valve is opened, when the rotor does not yet reach high rotational speeds, it can be attributed to the sudden pulse that the compressor receives as soon as the valve is opened. In fact, at this moment the pressurized airflow of the QSS is impinged into the compressor causing the acceleration of the rotor. This sudden change, therefore, leads to the arising of great stress on the compressor casing. This initial peak grows with the increasing of the pressure, as Fig 6.26 shows. The green curve, related to higher pressure level displays an initial amplitude greater than the red curve, highlighting how this initial impulse is affected by the pressure set in the pressure regulator, which acts on the airflow as a result.

The increase of the pressure set in the pressure regulator induces the casing of the compressor to experience a higher vibration field, which is certainly more intense in the dynamic case where the effect of rotation causes additional stresses; This is evident comparing the vibration amplitude gained the static tests S001, S002, and S003, displayed in Fig 6.22 with the results in Fig 6.26, concerning the dynamic tests D001, D002, and D003.

Chapter 7

Summary and Outlook

The experimental investigation conducted during this work of thesis has been developed to analyze the possible correlation between the damage occurred into the stator blade and the excitement workload induced by the QSS. Firstly a numerical analysis has been conducted using the finite element procedure on the stator blade geometry, and the first ten natural frequencies concerning the vibration modes of the blade have been acquired. Through the visualization of the results, it was possible to investigate the relative mode shapes, gaining important information regarding the behavior of the blade and its deformation. After the first part of numerical evaluations, the real core of the investigation work has involved the experiments conducted on the test rig, which comprises the compressor section of the engine, the QSS, and all the sensors from which the vibration measurements were acquired. To have a broader view of the vibration field that is generated due to the action of the QSS, the experimental analysis has involved the stator blades, the compressor casing, and the rear bearing placed on the shaft. These parts were instrumented with proper sensors, whose signals have been acquired and investigated to gain the vibration amplitude and evaluate the related spectrum of frequencies. The investigation of the blade behavior has shown that the main mode of deformation is the bending mode, which arose due to the exciting force induced by the QSS. This action is connected with a portion of airflow impinged by the three de Laval nozzles, that is reversed into the compressor, leading to the excitation of the blades, in particular those placed in the last stator stage, most exposed to the backflow action. The results have displayed that, as the pressure field inside the compressor increases, the mass flow rate through it grows accordingly, leading to an intensification of the vibration field involving the blades. This effect, combined with the vibration induced by the rotor dynamics, generates the arise of severe excitations into the compressor blades, more intense for the sixth compressor stage, exactly where the damage of the blade has occurred. The analysis of the results gained through the vibration sensors placed on the compressor casing and the rear bearing shows an intense

field of vibrations, involving both of them. In particular, the vibrations affecting the bearing show an amplitude which grows as the speed of the rotor increases, and persisting behavior even when the QSS is deactivated. Besides, the results concerning the compressor casing show that the most exciting point is when the coaxial valve of the QSS is opened and the rotor accelerated. This phenomenon acts on the compressor casing with a very high and sudden impulse. This investigation has led to the conclusion that although the QSS induces a significant reduction into the starting time of the second engine during ISEO, its impulsive nature originates harsh vibrations on the whole compressor, which could affect the life of the compressor and lead to the rise of fatigue phenomena. The results of this first investigative analysis represent the starting point for further evaluations and improvements, which will be the subjects of future studies, with the aim to reduce the extreme workload to which the compressor is exposed due to the QSS action.

Bibliography

- [1] ACAM MESS ELECTRONIC GMBH: *Rotational Speed Measurement System for Turbochargers*, April 2017
- [2] AFFONSO, L. O. A.: *Turbomachinery Blades*, 2006
- [3] BATHE, K. J.: *Finite Element Procedures*, 2016
- [4] BEBESEL, M. ; ALASCIO, A. D. ; SCHNEIDER, S. ; GUENTHER, S. ; VOGEL, F. ; WEHLE, C. ; SCHIMKE, D. : *Bluecopter Demonstrator An Approach To EcoEfficient Helicopter Design*, 2015
- [5] CEC VIBRATION PRODUCTS: *4-123 Vibration Transducer*, 2018
- [6] HBM: *Welcome to the webinar: welcome to the webinar An Introduction to Measurements using Strain Gauges*. <https://www.hbm.com/en/7039/webinar-an-introduction-to-measurements-using-strain-gauges/>. Version: 28.05.2020
- [7] HÖNLE, J. ; BARTH, A. ; ERHARD, W. ; KAU, H.-P. : *Engine Quick start in case of emergency – A requirement for saving fuel by means of engine shutdown*, September 4th/7th 2012.
- [8] HULL, L. ; SANTO, H. : *Development of a Rapid-Start System for the Boeing Model 502-2E Gas Turbine Engine.*, 1967
- [9] IDS INNOMIC GMBH : *Industrial Accelerometers IEPE*, February 2017
- [10] KERLER, M. ; LANG, S. ; FAUNER, T. ; ERHARD, W. : *Experimental Investigations of Rotating Stall and Surge in the Compressor System of a High-Speed Turbo-Shaft Engine*, September, 2014
- [11] KERLER, M. ; SCHÄFFER, C. ; ERHARD, W. : *Design of an engine quick-start system for rotorcraft application*, Diss., 2015

-
- [12] KERLER, M. ; SCHÄFFER, C. ; ERHARD, W. ; GÜMMER, V. : *Design of an airworthy turboshaft engine quick-start system with compact pressurized air supply for rotocraft application*, 2016
- [13] KERLER, M. ; SCHÄFFER, C. ; ERHARD, W. ; GÜMMER, V. : *Experimental Investigation of an Engine Quick-Start System with Compact Air Supply for Rotorcraft Application*, 2017
- [14] LEXIKON DER FLUGZEUGE UND HUBSCHRAUBER VON WOLFGANG BREDOW: *Antriebsarten für Flugzeuge und Hubschrauber*. http://www.bredow-web.de/Triebwerke_und_Flugzeugmotore/Allison_250/allison_250.html. Version: 26.03.2020
- [15] LFTA INGENIEURBUERO FUER THERMOAKUSTIK GMBH: *OMDS user Manual*, 2009
- [16] LILLO, S. A. ; LORIS: *Konstruktion und Erprobung eines Einblasegehäuses für ein Triebwerksschnellstartsystem, Masterarbeit*, 2019
- [17] MATWORKS DOCUMENTATION: *The Physics of the Damped Harmonic Oscillator*. <https://ch.mathworks.com/help/symbolic/examples/physics-damped-harmonic-oscillator.html>. Version: 20.05.2020
- [18] MIT: *Defining an analysis*. <https://abaqus-docs.mit.edu/2017/English/SIMACAEANLRefMap/simaanl-c-over.htm>. Version: 15.05.2020
- [19] MORI, Y. : *Mechanical Vibrations: Applications to Equipment*, February 2017
- [20] MYKLESTAD, N. O.: *Fundamentals of Vibration Analysis*, 2018
- [21] NEWLAND, D. E.: *Vibration Analysis and Computation*, , University of Cambridge, 1989
- [22] RODGERS, C. : *Impingement Starting and Power Boosting of Small Gas Turbines*, 1985
- [23] SPIESS, C. ; KERLER, M. ; M.HAJEK: *Effects On Helicopter Dynamics In Case Of Engine Failure During Intended Single Engine Operation*, 2014
- [24] TECHNICAL UNIVERSITY OF MUNICH: *Allison Gasturbinenprüfstand*. <https://www.lrg.tum.de/en/lrf/research/facilities/wellenleistungsgasturbine-i-allison-250/>. Version: 02.04.2020

- [25] THERMOMETRICS CORPORATION: *Thermometrics precision temperature sensors*.
<https://www.thermometricscorp.com/thertypk.html>. Version: 21.05.2020
- [26] TOKYO MEASURING INSTRUMENTS LAB: Cryogenic temperature series CF strain gauges, 2011
- [27] WIKA ALEXANDER WIEGAND SE & Co. KG: *Pressure transmitter for general industrial applications Model A10*, 2017